




Ultrafast dynamics of photoinjected electrons at the nonthermal regime in the intra- Γ -valley relaxation in InP studied by time- and angle-resolved photoemission spectroscopy

Katsumi Tanimura ^{1,*}, Hiroshi Tanimura ², and Jun'ichi Kanasaki ³

¹*The Institute of Scientific and Industrial Research, Osaka University, 8-1 Mihogaoka, Ibaraki, Osaka 567-0047, Japan*

²*Institute for Materials Research, Tohoku University, 2-1-1 Katahira, Sendai 980-8577, Japan*

³*Department of Mechanical and Physical Engineering, Graduate school of Engineering, Osaka-City University, 3-3-138 Sugimoto, Sumiyoshi, Osaka 565-8585, Japan*



(Received 6 March 2022; revised 9 August 2022; accepted 1 September 2022; published 16 September 2022)

We study ultrafast relaxation of photoinjected electrons confined within the Γ valley of InP, based on the transient electron distribution functions determined using time- and angle-resolved photoemission spectroscopy. To elucidate fundamental processes that lead to the quasithermalization of electron subsystem at the nonthermal regime of relaxation, the dynamics are investigated in two p -type samples with different doping levels, which exhibit different energy-relaxation rates of energetic electrons. In both samples, the photoinjected nonthermal-electron distributions are quasithermalized only at a finite time delay of several hundreds of femtoseconds. Although the magnitude of the time delay for quasithermalization depends on the initially prepared nascent electron distribution and on the energy-relaxation rates in different samples, the quasithermalization is established at the specific electron distribution of ensembles; electrons with a density of $\sim 1 \times 10^{17} \text{ cm}^{-3}$ are condensed in the phase space characterized by the maximum energy of 0.27 eV and by the maximum wave vector of 0.09 \AA^{-1} . The essential features of quasithermalization observed in InP are the same as those recently reported for GaAs [Phys. Rev. B **104**, 245201 (2021)], showing that the delayed quasithermalization is general for electrons photoinjected by ultrashort-laser excitation in the Γ valley of direct-gap semiconductors.

DOI: [10.1103/PhysRevB.106.125204](https://doi.org/10.1103/PhysRevB.106.125204)

I. INTRODUCTION

Ultrafast scattering of energetic carriers in semiconductors has been a strategic research field during the past three decades, as it constitutes the key process that determines functional limits and properties of micro-, nano- and opto-electronics [1–5]. For over 40 years, ultrafast optical spectroscopy has been developed to study dynamics of scattering processes, and the accumulating knowledge has provided a sound basis on which one can gain deeper insight into a variety of ultrafast phenomena in photoexcited semiconductors [3–5]. However, clear understanding of the physics involved in some incoherent dynamic scattering processes remains elusive due to the high complexity of the problem and partly due to methodological limitations to capture the scattering dynamics unambiguously.

The relaxation processes in semiconductors excited with an ultrashort laser pulse can be classified into four temporally overlapping regimes: (a) coherent, (b) nonthermal, (c) hot-carrier, and (d) isothermal regimes [3]. Among them, at the nonthermal regime, where the well-defined phase relationship between the excitation in the semiconductor and electromagnetic field is destroyed through dephasing, several incoherent scattering processes bring the photoinjected nonthermal electron distribution to a hot quasithermalized distribution [3]. To elucidate how and when the quasithermalization (thermaliza-

tion only within the electron subsystem) is established, it is crucial to trace the dynamics of incoherent scattering processes, based on the time (t)-dependent electron distribution function $f_e(k, E, t)$, resolved in momentum (k) and energy (E) spaces [4].

In the optical spectroscopies, the most typical methods to determine $f_e(k, E, t)$ at the femtosecond-temporal regime are the spectroscopy of the transient absorption saturation [3,6,7] and time-resolved band-to-band luminescence spectroscopy [8–10]. In both methods, optical signals associated with $f_e(k, E, t)$ are measured in momentum-integrated forms, and changes in spectral shapes and signal intensities are governed by both $f_e(k, E, t)$ and transient-hole distribution $f_h(k, E, t)$, particularly at short temporal domains [9,11]. Therefore, $f_e(k, E, t)$ has been inferred indirectly, using theoretical modeling with several approximations and parameters, which makes the obtained $f_e(k, E, t)$ less unambiguous.

On the other hand, time- and angle-resolved photoemission spectroscopy (TR-ARPES) can probe $f_e(k, E, t)$, with two advantages over optical spectroscopy [12]. The first is the capability of resolving the electron distributions in momentum space [12,13], and the second is that the method can probe $f_e(k, E, t)$ selectively without any contributions of $f_h(k, E, t)$ [14,15]. When the matrix-element effect on the photoemission process is well characterized [16–18], $f_e(k, E, t)$ can be determined experimentally (see Appendix A). Therefore, TR-ARPES offers a powerful method to explore the incoherent scattering dynamics of energetic electrons in the conduction band (CB) of semiconductors.

*tanimura@sanken.osaka-u.ac.jp

The scattering dynamics of energetic electrons injected into the Γ valley of the CB depends critically on the excess energy E_{ex} , referenced to the CB minimum (CBM) because of the drastically dependent modes and rates on E_{ex} of electron-phonon (e-ph) interactions [3,19–23]. Due to the prevalence of multivalley structures in the CB of semiconductors, the intervalley scattering among Γ , L , and X valleys plays a dominant role in the relaxation processes of electrons with sufficient E_{ex} [3]. On the other hand, for photoinjected electrons in the Γ valley into the states with E_{ex} lower than the minima of subsidiary valleys in direct-gap semiconductors, the scattering processes are confined in the central Γ valley; no intervalley scatterings are induced. When E_{ex} is smaller than the bandgap energy E_G , relaxation is free from complicated impact ionization processes which have been studied in InSb [24]. The scattering process of photoinjected electrons is then governed by the electron-electron (e-e), electron-hole (e-h), and electron-phonon (e-ph) interactions, which act competitively and/or cooperatively. Despite extensive optical studies on this topic [3–5], our understanding of scattering dynamics at the nonthermal regime of intra- Γ -valley relaxation is still incomplete.

In previous time-resolved band-to-band luminescence studies, complemented by Monte Carlo simulations, it was concluded that the quasithermalization of photoinjected electrons in the Γ valley is established within 100 fs under the excitation density ρ_0 ranging from 1×10^{17} to $7 \times 10^{17} \text{ cm}^{-3}$ in both GaAs and InP [8–10]. In these studies, it was emphasized that the internal thermalizations of the electron and hole subsystems occur in <100 fs. On the other hand, TR-ARPES has been applied recently to study the ultrafast dynamics at nonthermal regime in the intra- Γ valley relaxation in GaAs [18]. It has been demonstrated, based on the experimentally determined $f_e(k, E, t)$, that the quasithermalization of photoinjected electrons in p -type GaAs is established only after time delays of several hundred femtoseconds under ρ_0 ranging from 1.5×10^{16} to $5 \times 10^{17} \text{ cm}^{-3}$. Although the quasi-equilibration in the momentum space is achieved within 100 fs of excitation by the e-e interaction among photoinjected electrons, the quasithermalization of the electronic system evolves in such a way that a substantial part of the electronic energy is dissipated to other subsystems via the e-ph and e-h interactions until the electron distributions ideal for the quasithermalization are prepared [18]. The TR-ARPES study has revealed a characteristic of intravalley relaxation dynamics which is different from those proposed previously.

In this paper, using TR-ARPES, we revisit the ultrafast relaxation dynamics of photoinjected electrons in the intra- Γ -valley relaxation in InP, another prototypical direct-gap semiconductor. The bulk electronic structures of InP are like those of GaAs. The E_G of InP (GaAs) is 1.42 eV (1.52 eV), and the CB is characterized by the effective mass $m^* = 0.080m_e$ ($0.067m_e$), where m_e is the electron rest mass [25,26]. However, the polaron coupling constant of electrons in the CB in InP is ~ 1.5 times larger than that in GaAs, and energy relaxation rate by the Fröhlich interaction in InP is 2.2 times higher than that in GaAs [25]. Therefore, InP is one of the best samples to study the characteristics of the intra- Γ -valley relaxation of energetic electrons comparatively with those obtained for GaAs in Ref. [18]. The results will give a clear

answer whether the delayed quasithermalization of the electron subsystem in the Γ -valley relaxation is specific to GaAs or it is more general in other direct-gap semiconductors. They will also provide valuable information on the characteristic features of nonthermal regime in the Γ -valley relaxation in direct-gap III–V semiconductors in general.

II. EXPERIMENTAL METHODS

Two single crystals of p -type InP (p -InP), doped with Zn at different doping levels, were used. One sample (p -InP#1) with the hole concentration h_0 of $1.5 \times 10^{17} \text{ cm}^{-3}$ was grown via the vertical gradient freeze method (purchased from MTI), and the other (p -InP#2) with $h_0 = 6.6 \times 10^{18} \text{ cm}^{-3}$ was grown via the liquid encapsulated Czochralski method (purchased from SurfaceNet GmbH). They were cleaved under ultrahigh vacuum conditions ($<5 \times 10^{-11}$ Torr), and surface structures were characterized *in situ* using a scanning tunneling microscope. All samples showed well-ordered (1×1) surface structure, and concentrations of surface point defects were typically $<10^{-3}$ monolayers. A 76 MHz Ti-sapphire laser generated 75 fs laser pulses centered at photon energies from 1.4 to 1.70 eV. A portion of the fundamental output was converted to third-harmonic pulses for probing photoemission. The cross-correlation trace between pump and probe pulses in a β -barium borate crystal was well described by a Gaussian with a full width at half maximum of 110 ± 10 fs. The probe pulses passed a computer-controlled delay stage to set the time delay (Δt) with respect to the pump pulses, and pump and probe pulses were aligned coaxially and focused on the sample surfaces at 45° to surface normal. The typical spot size of pump (probe) pulses was 9.0×10^{-5} (1.4×10^{-5}) cm^2 . The pump-pulse fluence was set to give an excitation density ρ_0 of $1.0 \pm 0.1 \times 10^{17} \text{ cm}^{-3}$, which was evaluated using the formula: $\rho_0 = F_p(1-R)\alpha$, with the photon fluence of pump pulse F_p , the reflectivity R , and the absorption coefficient α at excitation photon energy $h\nu_{\text{pump}}$. Probe-pulse fluences were $< \frac{1}{500}$ of those of pump pulses. Using a hemispherical electron analyzer operated in an angle-resolved lens mode, equipped with a charge-coupled device detector, photoelectron images were recorded as a function of the photoelectron energy E_{mes} referenced to the work function of the analyzer and emission angle θ along the [001] crystal direction: surface normal photoemission was along the [110] crystal direction. The energy resolution was 55 ± 5 meV, while the angle resolution was $\pm 0.5^\circ$.

On the vacuum-cleaved (110) surface of InP, like other III–V semiconductors, no surface reconstructions are induced, but the surface atoms are relaxed normal to the surface from their positions in a bulklike layer within the first two layers of the surface with a typical depth of ≈ 0.2 nm, keeping the dimensions of the unit cell unchanged [27]. These features of surface relaxation of the (1 1 0)-(1 \times 1) result in the following three characteristics of low-energy photoemission [18]. The first is that no backfoldings of the electronic states occurs [28], which makes band assignment unambiguous. The second is that no surface band-bending effects are induced on this surface, as intrinsic surfaces states do not exist in the bandgap energy region [27]. Surface point defects, e.g., anion monovacancies can act as the pinning centers of the

Fermi level when the concentration exceeds 10^{-2} monolayers [29]. However, the defect concentration is $<10^{-3}$ monolayers, as determined by a scanning tunneling microscope, ensuring the flat-band condition. In fact, the vacuum level at the surface, which is sensitive to the band bending and hence the surface photovoltaic effects [27,30], stayed constant within a few millielectronvolts for the Δt ranging from -10 to 50 ps. The third is the enhanced bulk sensitivity. In this paper, we used the probe-photon energy $h\nu_{\text{probe}}$ ranging from 4.6 to 5.2 eV. The photoemission by $h\nu_{\text{probe}}$ as low as 5 eV takes place with the escape depth of >3 nm, which is much longer than the depths (~ 0.5 nm) in normal ultraviolet photoemission spectroscopy probed by light with photon energy of typically a few tens of electronvolts [27,31]. As the depth of modification (~ 0.2 nm) by the surface relaxation on InP(110)-(1 \times 1) is small compared with the escape depth of the photoelectrons probed by the low-energy photons, the bulk sensitivity is enhanced strongly by the volume effect.

III. EXPERIMENTAL RESULTS

Figures 1(a) and 1(b) show the energy- and momentum-resolved (k -resolved) maps of photoemissions for p -InP#1 measured at $\Delta t = 20$ fs and 4.5 ps under p -polarized 1.70 eV light pulses at 293 K and $\rho_0 = 1.0 \times 10^{17}$ cm $^{-3}$. In the figures, photoemission intensities specified by color scales are plotted as a function of k_{\parallel} and E_K on the left-side scale (see Appendix A for the determination of E_K). The electronic structures and the dynamics of energetic electrons in the CB are most conveniently characterized by the excess energy E_{ex} referenced to the CBM. The right-side scale, which is the same as the scale in Fig. 1(d), represents the initial-state energy of photoemission in terms of E_{ex} , evaluated by the relation $E_{ex} = E_K + \chi - h\nu_{\text{probe}}$, where χ is the electron affinity ($=\Phi_{\text{vac}} - E_G$).

In the photoemission measurements, the [110] crystal axis is aligned along the surface normal (z), and the x and y axes correspond to the [001] and [1 $\bar{1}$ 0] directions. Under this geometry, the bulk Brillouin zone (BBZ) and the surface Brillouin zone (SBZ) have the relation shown in Fig. 1(c) [13,28]. As the emission angle corresponds to k_{\parallel} along the $\bar{\Gamma}-\bar{Y}$ ($=\bar{X}'$) direction of the SBZ, the measured photoemission image represents a one-dimensional cut, along $\bar{\Gamma}-\bar{Y}$ of the SBZ, of the two-dimensional projection of three-dimensional electron distributions. The projection has the following characteristics. First, all states along the $\bar{\Gamma}-\bar{K}$ direction in the BBZ are projected at $\bar{\Gamma}$, contributing to surface-normal photoemission. Second, the states along the $\bar{\Gamma}-\bar{L}$ line in the BBZ are projected on the $\bar{\Gamma}-\bar{Y}$ direction with k_{\parallel} given by $k_{\parallel} = k_L \cos(54.7^\circ)$, with k_L being the wave vector along the $\bar{\Gamma}-\bar{L}$ direction. Third, the states along the $\bar{\Gamma}-\bar{X}$ line in the BBZ are projected on the $\bar{\Gamma}-\bar{Y}$ direction with $k_{\parallel} = k_X$, with k_X being the wave vector along the $\bar{\Gamma}-\bar{X}$ direction. Therefore, the photoemission images measured in this paper capture photoelectrons emitted from the initial states included in the projection plane shown in light blue (hereafter, we call the projection plane *the detection plane* for photoemission).

The determination of k_{\parallel} fixes a point on the two-dimensional SBZ; the momentum k_{\perp} normal to the surface

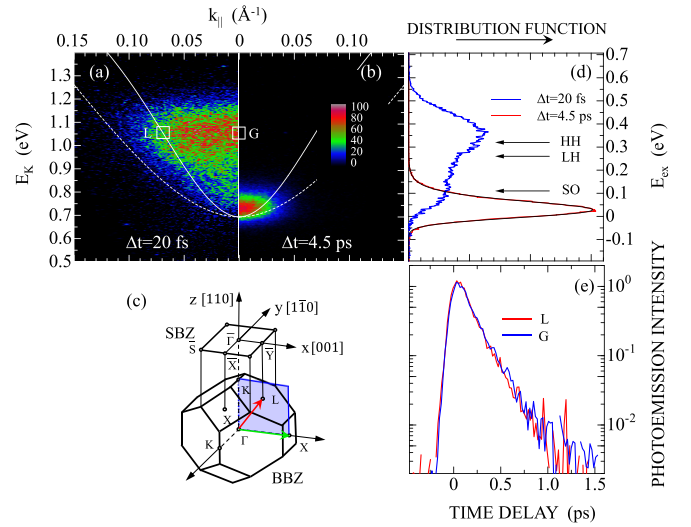


FIG. 1. Images of photoemission from p -InP#1 measured at (a) $\Delta t = 0$ fs and (b) $\Delta t = 1.5$ ps under excitation with p -polarized 1.70 eV light pulses at 293 K. The intensities, specified by the color scale, are plotted as a function of k_{\parallel} and E_K (left vertical axis). The solid and broken curves show the conduction band dispersion along $\bar{\Gamma}-\bar{L}$ and $\bar{\Gamma}-\bar{X}$ directions, plotted as a function of k_{\parallel} , based on the band structure calculation in Ref. [32]. (c) The relation between the surface and bulk Brillouin zones for InP with the (110) surface under the present experimental geometry. The plane (light blue) is the detection plane, and the red (green) arrow within the plane shows the direction from the $\bar{\Gamma}$ to \bar{L} ($\bar{\Gamma}$ to \bar{X}) points. (d) The spectra of normal photoemission ($k_{\parallel} = 0 \pm 0.005 \text{ \AA}^{-1}$) of the images shown in (a) and (b) plotted as a function of E_{ex} . The solid black curve shows the Maxwell distribution function with $T_e = 300$ K convolved with respect to the finite energy resolution of 55 meV. The arrows labeled heavy hole (HH), light hole (LH), and split off (SO) are the final-state energies of optical transitions from the HH, LH, and SO valence band induced by 1.70 eV photons, based on the band calculation in Ref. [32]. (e) Temporal changes in photoemission intensities at energy- and momentum-resolved points L and G indicated by the rectangles in (a). Intensities are normalized at maxima of respective curves and plotted on a semilogarithmic scale.

can have a value anywhere along the rod extending into the three-dimensional BBZ [28]. Therefore, the off-normal photoemission detected experimentally at a given k_{\parallel} is a superposition of many contributions from such states that are projected on the one-dimensional cut along the $\bar{\Gamma}-\bar{Y}$ direction of the SBZ. Under the present experimental geometry, the dispersion along the $\bar{\Gamma}-\bar{L}$ line displays the contribution to off-normal emissions from typical high-symmetry points. The solid (broken) curve in Figs. 1(a) and 1(b) is the CB dispersion along $\bar{\Gamma}-\bar{L}$ direction ($\bar{\Gamma}-\bar{X}$ direction) as a function of k_{\parallel} , evaluated using the theoretical results obtained in Ref. [32]. As the k_{\perp} is zero for states along the $\bar{\Gamma}-\bar{X}$ direction, photoemission from the states cannot be detected under the geometry; the curve along the $\bar{\Gamma}-\bar{L}$ line portrays the border of the low-energy part of the $\bar{\Gamma}$ valley.

To identify the initial states of photoemission unambiguously, we focus our attention to the normal photoemission; the normal photoemission spectrum reflects the electron distribution $f_e(\bar{\Gamma}, E_{ex}, \Delta t)$ along the $\bar{\Gamma}-\bar{K}$ line, a well-defined line

in the BBZ. For this purpose, the energy- and time-resolved normal photoemission intensity $I_e(\bar{\Gamma}, E_K, \Delta t)$, which is obtained by integrating photoemission intensities for $k_{\parallel} = 0 \pm 0.005 \text{ \AA}^{-1}$, is converted to the $f_e(\bar{\Gamma}, E_{ex}, \Delta t)$ by correcting the matrix-element effects using the method described in Appendix A.

The $f_e(\bar{\Gamma}, E_{ex}, \Delta t)$ thus obtained from the images in Figs. 1(a) and 1(b) are plotted in Fig. 1(d) as a function of E_{ex} . The experimentally determined distribution at $\Delta t = 4.5 \text{ ps}$ is well described by the Maxwell distribution function with $T_e = 300 \text{ K}$ (because of the low ρ_0 , the thermalized electron distribution near CBM is approximated by Maxwell distribution function). On the other hand, the $f_e(\bar{\Gamma}, E_{ex}, \Delta t)$ at $\Delta t = 20 \text{ fs}$ shows a strong nonthermal feature; the populations at high-energy states are significantly higher than at low-energy states. Based on the theoretical band structure in Ref. [32], we can estimate the energies of the CB states reached by the optical transitions at Σ along the Γ - K direction from the heavy-hole (HH), light-hole (LH), and split-off (SO) valence band induced by the 1.70 eV pump light; it is 0.32, 0.26, and 0.11 eV from the CBM as indicated by arrows. The estimated energies can reasonably characterize the spectral feature of the distribution $f_e(\bar{\Gamma}, E_{ex}, 20 \text{ fs})$. Therefore, we conclude that $f_e(\bar{\Gamma}, E_{ex}, 20 \text{ fs})$ represents the nascent electron distribution along the Γ - K line injected by p -polarized 1.70 eV light excitation. As the minimum of the L valley is located 0.59 eV above the CBM [26], the energetic electrons are photoinjected into the states lower than the minimum of the L valley; the scattering processes of these electrons are confined in the central Γ valley, resulting in intra- Γ -valley relaxation.

Under the present geometry of photoemission measurements, the polarization selection rule [33] predicts that the transitions from the HH (LH) band are allowed only for s (p)-polarized light at Σ along the Γ - K line. The rule predicts also that the transition from the HH band at Λ along the Γ - L line, which contributes to the off-normal photoemission, is allowed for both s - and p -polarized light. Consequently, it is predicted that the off-normal emission intensities are stronger than the normal emission intensities at the energy region of the HH-band transitions for the p -polarized light. These predictions by the polarization selection rules have been beautifully demonstrated in TR-APRES studies using $h\nu_{\text{pump}} > 2.0 \text{ eV}$ [13]. However, as seen in Fig. 1(a), the photoemission intensities at $E_{ex} = 0.35 \text{ eV}$ are almost constant, irrespective of k_{\parallel} , which is contradictory to the prediction by the optical selection rule. We presume that the difference comes from the scattering dynamics after photoinjection rather than the breakdown of the polarization selection rules, like the case in GaAs discussed in Ref. [18].

The electrons photoinjected in the Γ valley into the states energetically higher than the minimum of the L valley are quasi-equilibrated in the whole momentum space including Γ , L , and X valleys within a few tens of femtoseconds by the strong e-ph interactions [13,19]. The rates of e-ph interactions for electrons confined in the Γ valley are very low due to a small final density of states for e-ph scatterings [19–23]. However, they are subject to the ultrafast momentum scattering by the e-e interaction [25,34], by which the initial momentum distributions gained from external fields are randomized to generate the quasi-equilibrated distributions

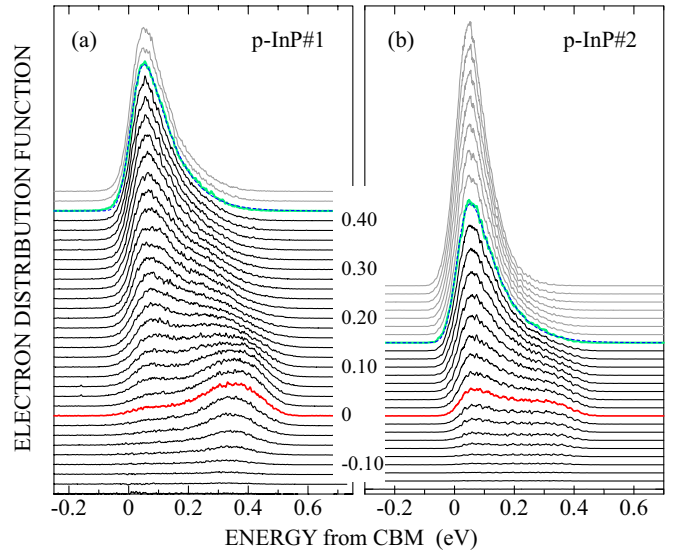


FIG. 2. Temporal evolution of electron distribution functions along the Γ - K line in p -InP at 293 K under s -polarized 1.70 eV excitation in two different samples. The distribution function is presented with a constant offset to the base line for each Δt indicated by number (in units of picoseconds). The red curves show the spectra at $\Delta t = 0 \text{ ps}$, while the green curves show the distributions at which quasithermalization is established. The broken blue curves, at (a) $\Delta t = 0.42 \text{ ps}$ and (b) $\Delta t = 0.17 \text{ ps}$ show the electron distributions given by the Maxwell distribution function with $T_e = 800 \text{ K}$.

only in the momentum space. In Fig. 1(e), temporal changes in photoemission intensities are compared at two different energy- and momentum-resolved points labeled L and G in Fig. 1(a); they show essentially the same changes. The results support that the nonthermal electrons with a given E_{ex} [$=0.35 \text{ eV}$ in the case of Fig. 1(e)] are quasi-equilibrated in the momentum space within a pump-pulse width. In contrast to the ultrafast quasi-equilibration in the momentum space, the quasithermalization of photoinjected electrons in energy space takes place at a longer timescale, as shown below.

In Fig. 2, the temporal evolution of $f_e(\bar{\Gamma}, E_{ex}, \Delta t)$ under s -polarized 1.70 eV excitation at $\rho_0 = 1.0 \times 10^{17} \text{ cm}^{-3}$ is displayed for two InP samples with different doping levels: Fig. 2(a) for p -InP#1 ($h_0 = 1.5 \times 10^{17} \text{ cm}^{-3}$) and Fig. 2(b) for p -InP#2 ($h_0 = 6.6 \times 10^{18} \text{ cm}^{-3}$). In both figures, the solid red curves show the distributions measured at $\Delta t = 0 \text{ fs}$. In Fig. 2(a), the distribution around $\Delta t = 0 \text{ fs}$, featured by the largest population around $E_{ex} = 0.35 \text{ eV}$, is transferred to form a two-peak structure with roughly the same heights $\sim 100 \text{ fs}$ of excitation. At $\Delta t > 200 \text{ fs}$, the electron population is further accumulated near the CBM and forms a single distribution with a high-energy tail. The spectral-shape analysis, based on the relation between the peak energy and the asymmetry of $f_e(\bar{\Gamma}, E_{ex}, \Delta t)$ [18,35], has shown that the distribution is quasithermalized at $\Delta t = 420 \pm 20 \text{ fs}$ with $T_e = 800 \pm 20 \text{ K}$. The distribution at $\Delta t = 420 \text{ fs}$, shown by green curve, is well fitted to the Maxwell distribution function with $T_e = 800 \text{ K}$ (broken blue curve). On the other hand, in p -InP#2, the two-peak structure of the distribution is already clear at $\Delta t = 0 \text{ fs}$, and the quasithermalized distribution is

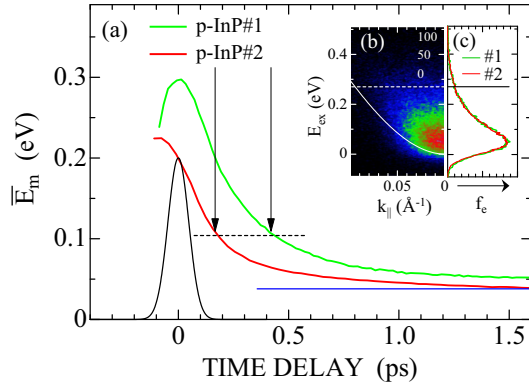


FIG. 3. (a) Temporal changes in the mean energy of electron distribution functions along the Γ - K line under 1.70 eV excitation at $\rho_0 = 1.0 \times 10^{17} \text{ cm}^{-3}$ in p -InP#1, green curve, and in p -InP#2, red curve. The blue line indicates the mean energy $[(\frac{3}{2})k_B T_e]$ of the Maxwell distribution at 293 K. The black arrows show the time delays when the quasithermalization is achieved. (b) The energy- and momentum-resolved photoemission image at $\Delta t = 420$ fs in p -InP#1. The photoemission intensities, specified a color scale, are plotted as a function of E_{ex} and k_{\parallel} . The solid curve shows the conduction band (CB) dispersion along the Γ - X direction. The broken line shows the level of $E_{ex} = 0.27$ eV. (c) The electron distribution function along the Γ - K line at $\Delta t = 420$ fs in p -InP#1, green curve, and that at $\Delta t = 166$ fs in p -InP#2, red curve.

established at 170 ± 20 fs. The spectrum at $\Delta t = 166$ fs, shown by the green curve in Fig. 2(b), is well described by the Maxwell distribution function with $T_e = 800$ K (broken blue curve). Although the general feature in temporal evolution of $f_e(\bar{\Gamma}, E_{ex}, \Delta t)$ is like the case of p -InP#1, it appears that the energy-relaxation rates of photoinjected energetic electrons in p -InP#2 are substantially higher than in p -InP#1, leading to the faster quasithermalization of electron subsystem.

To gain deeper insight into the difference in relaxation processes in the two samples, we examine the temporal evolution of the mean energy \bar{E}_m defined as

$$\bar{E}_m(\Delta t) = \frac{\int_{-\infty}^{\infty} E f_e(\bar{\Gamma}, E, \Delta t) dE}{\int_{-\infty}^{\infty} f_e(\bar{\Gamma}, E, \Delta t) dE} \quad (1)$$

for the electron ensemble characterized by $f_e(\bar{\Gamma}, E, \Delta t)$. The evaluated \bar{E}_m is plotted in Fig. 3; the green (red) curve shows the result of p -InP#1 (#2). In p -InP#1, $\bar{E}_m = 0.30$ eV just after the excitation, which represents the \bar{E}_m of the nascent photoinjected electron ensemble. It decreases rapidly within 1 ps of excitation and reaches a roughly constant value of 0.05 eV around $\Delta t = 1.5$ ps. On the other hand, the maximum value of \bar{E}_m in p -InP#2 is lower than that in p -InP#1, and it starts to decrease within the cross-correlation width of 110 fs, shown by the black curve, toward a constant value around $\Delta t = 1.5$ ps.

It should be emphasized that the quasithermalization of photoinjected electrons is established at the same \bar{E}_m (≈ 0.10 eV), despite a significant difference in relaxation rates in two samples. Figure 3(b) shows the photoemission image in p -InP#1 at $\Delta t = 420$ fs when the electron distribution is quasithermalized. The image is representative

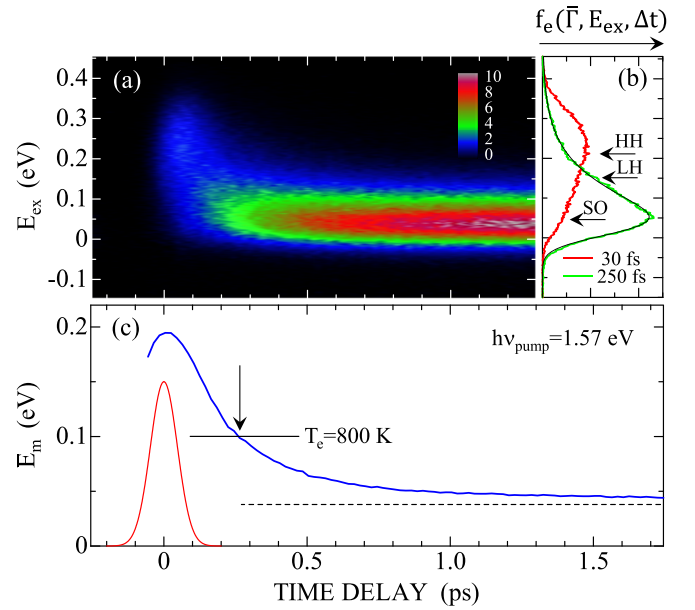


FIG. 4. (a) Temporal evolution of the electron distribution function along the Γ - K line under 1.57 eV excitation. The height of $f_e(\bar{\Gamma}, E_{ex}, \Delta t)$, indicated by a color scale, is displayed as a function of Δt and E_{ex} . (b) The electron distribution functions at $\Delta t = 30$ fs, red, and $\Delta t = 250$ fs, green. The solid black curve shows the Maxwell distribution function at $T_e = 800$ K. The arrows labeled heavy hole (HH), light hole (LH), and split off (SO) indicate the estimated energy levels of the conduction band (CB) states reached by the optical transitions from the HH, LH, and SO valence band induced by the 1.57 eV pump light, based on the band calculation in Ref. [32]. (c) Temporal changes in the mean energy of electron distribution functions along the Γ - K line under 1.57 eV excitation. The arrow indicates the time delay when the quasithermalization is achieved. The red curve shows the cross-correlation between the pump and probe pulses. The broken line indicates the mean energy $[(\frac{3}{2})k_B T_e]$ of the Maxwell distribution at 293 K.

of the electron distribution in momentum and energy spaces when the quasithermalization is established. In Fig. 3(c), the green curve shows the $f_e(\bar{\Gamma}, E, \Delta t)$ at $\Delta t = 420$ fs in p -InP#1, while the red curve shows the $f_e(\bar{\Gamma}, E, \Delta t)$ at $\Delta t = 166$ fs in p -InP#2. The two distributions are essentially identical. The result implies that the quasithermalization is established when a specific distribution of energetic-electron ensemble is formed during relaxations. In this distribution, typically 95% of photoinjected electrons are confined in the CB states below $E_{ex} = 0.27$ eV with wave vectors $< 0.09 \text{ \AA}^{-1}$.

To confirm the importance of the specific electron distribution for quasithermalization of photoinjected electrons in the Γ valley, we examined the relaxation process of energetic electrons with a different nascent distribution. Figure 4(a) shows the temporal evolution of $f_e(\bar{\Gamma}, E_{ex}, \Delta t)$ in p -InP#1 under s -polarized 1.57 eV excitation. The pump-pulse fluence was set to generate $\rho_0 = 1.0 \times 10^{17} \text{ cm}^{-3}$. The height of $f_e(\bar{\Gamma}, E_{ex}, \Delta t)$, indicated by a color scale, is displayed as a function of Δt and E_{ex} . In Fig. 4(b), $f_e(\bar{\Gamma}, E_{ex}, 30 \text{ fs})$ at $\Delta t = 30$ fs is shown by red curve, which is featured by nonthermal distribution with the peak ~ 0.25 eV. The arrows in the figure show the states in the CB predicted by transitions at

the Σ region from HH, LH, and SO valence bands for 1.57 eV photons based on the band diagram of Ref. [32]. The predicted energies can reasonably characterize the spectral features of $f_e(\bar{\Gamma}, E_{ex}, 30 \text{ fs})$, supporting our conclusion that the spectrum represents the nascent electron distribution induced by 1.57 eV excitation.

The rapid relaxation occurs within 300 fs, as shown in Fig. 4(a). In Fig. 4(c), temporal change in \bar{E}_m is shown. The maximum value of $\bar{E}_m = 0.20 \text{ eV}$ reached just after excitation is reduced rapidly within 300 fs of excitation and approaching the thermalized value of 0.03 eV ($1.5k_B T$ at $T = 293 \text{ K}$) at larger Δt . Spectral shape analysis shows that the distribution is quasithermalized at $\Delta t = 250 \pm 30 \text{ fs}$ when the magnitude of $\bar{E}_m = 0.10 \text{ eV}$, which is the same as that under 1.70 eV excitation shown in Figs. 2 and 3. The green curve in Fig. 4(b) shows the $f_e(\bar{\Gamma}, E_{ex}, 250 \text{ fs})$, which is well represented by the Maxwell distribution function with $T_e = 800 \text{ K}$ (solid black curve). The electron distribution in energy and momentum spaces, determined by the photoemission image at $\Delta t = 250 \text{ fs}$ under 1.57 eV excitation, shows that $\sim 95\%$ of photoinjected electrons are confined in the CB states below $E_{ex} = 0.27 \text{ eV}$, as in the case of 1.70 eV excitation.

IV. DISCUSSIONS

As shown in Sec. III, the quasithermalization of photoinjected energetic electrons in the CB is established when the energetic-electron ensembles are relaxed to the specific distribution during relaxation. The time necessary for quasithermalization, which depends on samples and on the nascent electron distributions, can be regarded as the period within which the specific distribution ideal for the quasithermalization is prepared. In this section, we discuss the relaxation dynamics more quantitatively to have deeper insight into the interactions responsible for the differences in quasithermalization times and to reveal characteristic features of the specific electron distribution for quasithermalization.

A. The relaxation of photoinjected nonthermal electrons and Fröhlich interaction in InP

The scattering process of photoinjected electrons with E_{ex} lower than the minimum of the L valley is confined in the Γ valley and is governed by the e-e, e-h, and e-ph interactions [3–5]. The e-e interaction, which is the primary source for establishing quasithermalization of the electron subsystem, plays the important role in the quasi-equilibration of photoinjected electrons in momentum space, as shown in Sec. III. However, the e-e interaction is not efficient enough to quasithermalize photoinjected nonthermal electron distribution in the same timeframe, and the quasithermalization is established only after a substantial amount of energy of the electron subsystem is transferred to other subsystems. The processes responsible for the electronic-energy loss are the e-ph and e-h interactions, both of which transfer the energy of the electron subsystem to other subsystems without reducing total density of electrons in the CB. The other processes that lead to the reduction of the density of energetic electrons from the detection region of photoemission can also contribute to the electronic-energy loss. However, as shown in Appendix

B, the contributions of these processes are small; $>80\%$ of photoinjected electrons remain in the CB within the timeframe of quasithermalization. As demonstrated in previous studies [3,7], the Fröhlich interaction plays the important role on electronic-energy relaxation in III–V semiconductors. We first discuss the role of this mechanism on the energy relaxation of nonthermal-electron relaxation in the Γ valley of InP.

The low-energy part of the CB in InP is approximated as a nonparabolic spherical band characterized by the effective mass m^* and the nonparabolicity constant α : $m^* = 0.080m_e$ [25,26] and $\alpha = 0.596$ [25]. For the electron with energy e_k (specified by the wave vector k) referenced to the CBM, the scattering rate $W(k)$ by the Fröhlich interaction is given by [25,36]

$$W(k) = W_0 I^2(k, k') [F_{em}(e_k) + F_{abs}(e_k)]. \quad (2)$$

In Eq. (2),

$$W_0 = \frac{e^2 \sqrt{2m^*} \omega_{LO}}{4\pi \hbar \epsilon_P}, \quad (3)$$

where \hbar is Planck's constant, ω_{LO} is the longitudinal optical (LO) phonon frequency, and $1/\epsilon_P = 1/\epsilon_\infty - 1/\epsilon_s$ with the high frequency ϵ_∞ and static ϵ_s dielectric constants. Here, $I(k, k')$ is the overlap integral of Bloch functions of initial (k) and final (k') states of the scattering, and $F_{em}(e_k)$ and $F_{abs}(e_k)$ are the e_k -dependent part of LO phonon emission and absorption rates given by

$$F_{em}(e_k) = \frac{[1 + n(\omega_{LO})] \left[\frac{d\gamma(e_k)}{de_k} \right]_{e_k - \hbar\omega_{LO}} \tanh^{-1} \left[\frac{\sqrt{\gamma(e_k - \hbar\omega_{LO})}}{\sqrt{\gamma(e_k)}} \right]}{\sqrt{\gamma(e_k)}}, \quad (4)$$

$$F_{abs}(e_k) = \frac{n(\omega_{LO}) \left[\frac{d\gamma(e_k)}{de_k} \right]_{e_k + \hbar\omega_{LO}} \coth^{-1} \left[\frac{\sqrt{\gamma(e_k + \hbar\omega_{LO})}}{\sqrt{\gamma(e_k)}} \right]}{\sqrt{\gamma(e_k)}}, \quad (5)$$

with the LO phonon occupation number $n(\omega_{LO})$, and $\gamma(e_k)$, which is defined as

$$\gamma(e_k) = e_k(1 + \alpha e_k). \quad (6)$$

The energy relaxation rate (de_k/dt) is then given by [25,36]

$$\frac{de_k}{dt} = (\hbar\omega_{LO}) W_0 I^2(k, k') [-F_{em}(e_k) + F_{abs}(e_k)]. \quad (7)$$

Although $I(k, k')$ is less than unity where nonparabolicity is present [25], we assume $I(k, k') = 1$ for simplicity. Under this assumption, the energy relaxation rate given by Eq. (7) becomes k independent; the rate is determined only by the excess energy ($e_k = E_{ex}$). The calculated result of Eq. (7) is shown as a function of E_{ex} by blue curve in Fig. 5. In the calculation, we used $\hbar\omega_{LO} = 43 \text{ meV}$ [37] and other material constants given in Ref. [25]. These parameters give $W_0 = 3.34 \times 10^{12} \text{ s}^{-1}$.

In Fig. 5, $-dE_{ex}/dt$ is 0.46 eV/ps for electrons with $E_{ex} > 0.2 \text{ eV}$, which predicts that the electronic energy of 0.1 eV is lost in the timeframe of 220 fs at the states with $E_{ex} > 0.2 \text{ eV}$. The red curve in the figure is the time-resolved electron distribution function in the CB at $\Delta t = 20 \text{ fs}$, which is obtained by correcting both the matrix-element effects and the k -dependent detection-efficiency effects of photoemission using

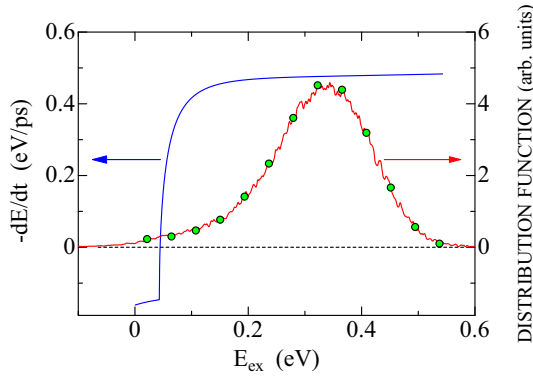


FIG. 5. Theoretical energy-relaxation rate for polar optical mode scattering of Γ -valley electrons in InP, calculated using Eq. (7), is plotted by blue curve as a function of excess energy. A spherical nonparabolic band, characterized by $m^* = 0.080m_e$ and $\alpha = 0.596$, is assumed for the conduction band (CB). Other material constants used in the calculation are as follows: $\hbar\omega_{LO} = 43$ meV, $\varepsilon_\infty/\varepsilon_0 = 9.52$, and $\varepsilon_s/\varepsilon_0 = 12.35$ (ε_0 being the permittivity of free space). The red curve shows the electron distribution function in the CB at $\Delta t = 20$ fs in p -InP#1, obtained by correcting the matrix-element and detection-efficiency effects (see Appendix B). The green circles represent the results of theoretical simulation; the amplitudes of N_j at $\Delta t = 20$ fs obtained by the simulation is plotted as a function of $E_j (= E_{ex})$ (see the text).

the method described in Appendix B. The electrons are distributed mostly at the states with $E_{ex} > 0.2$ eV. In Fig. 2, the populations at the states with $E_{ex} > 0.2$ eV are transferred to the states with $E_{ex} < 0.2$ eV within ~ 300 fs in p -InP#1, while a similar population transfer occurs within 160 fs in p -InP#2. The results suggest that the high rate of energy relaxation predicted by Eq. (7) is qualitatively consistent with the experimental results. However, to elucidate thoroughly the relative importance of several possible energy-relaxation mechanisms, more quantitative comparisons between the experimental results and theoretical consequences of the Fröhlich interaction are highly desirable, beyond such a qualitative argument.

For the quantitative comparison, there is one serious problem that the energy-relaxation rate which can be compared directly with Eq. (7) cannot be obtained in the present experiment, as the experimental conditions to generate energetic electrons are qualitatively different from those in the theoretical formalism. The theory assumes one single electronic state with energy e_k and two other states generated by LO phonon emission and absorption transitions with energies $e_k \pm \hbar\omega_{LO}$. The population n_k at the initial state with e_k decays with the time constant τ_k which is governed purely by the total LO phonon scattering rates at the state with e_k [given by Eq. (2)]. This ideal case may be applicable for the continuous wave (CW) luminescence spectroscopy for carrier relaxation in semiconductors, where a spectrally narrow CW laser shining onto a sample lifts electrons from the HH, LH, and SO bands into three narrow energy regions in the CB, and the relaxation forms the LO phonon cascade [38]. However, the present experimental situations under ultrashort laser excitation are far from the ideal case; energetic electrons with continuous broad distributions (as shown by red curve in Fig. 5) are introduced

simultaneously within a temporal period of pump-laser pulses. Then the population at the state with E_{ex} is strongly affected not only by the population loss by the scattering processes at E_{ex} but also by the population flows from other states with energy $E_{ex} \pm \hbar\omega_{LO}$ by LO phonon emission and absorption transitions. Under such *population-transfer cascades* by the LO-phonon-induced transitions, the dynamics of the population at the state with E_{ex} is modified strongly from the ideal dynamics predicted by the theory which derives Eq. (7).

In Fig. 3, we introduced \bar{E}_m , defined by Eq. (1), for examining energy relaxation. The first derivative of \bar{E}_m with respect to Δt gives a measure for the energy-relaxation rate at a given Δt . However, we cannot compare quantitatively the magnitudes of derivatives with the theoretical results shown in Fig. 5, as the \bar{E}_m is defined as an average over a whole excess-energy range, and temporal changes of populations at the energy-resolved states are possibly affected by the population-transfer cascade. Therefore, we need a different approach for more quantitative comparisons of the present results with theoretical consequences of the Fröhlich interaction.

B. Dynamics of energy-resolved electron-population densities

As an alternative approach to clarify the role of the Fröhlich interaction on the electron dynamics in the Γ -valley relaxation in InP, we analyze the dynamics of the time- and energy-resolved electron-population density $\rho_e(E_{ex}, \Delta t)$ in the CB. Theoretically, based on the formalism of the Fröhlich interaction described in Sec. IV A, we can simulate the dynamics of $\rho_e(E_{ex}, \Delta t)$ including the effects of the population-transfer cascade by the LO-phonon-induced transitions. Experimentally, we can determine $\rho_e(E_{ex}, \Delta t)$ using the results of temporal changes in photoemission intensities at a given E_K . Therefore, the quantitative comparison between the experimental and theoretical results of dynamics of $\rho_e(E_{ex}, \Delta t)$ makes it possible to examine the role of Fröhlich interaction on the nonthermal electron relaxation more thoroughly than in Sec. IV A.

We start with the theoretical simulations of the effects of the population-transfer cascade on the dynamics of $\rho_e(E_{ex}, \Delta t)$. For this purpose, we introduce a set of simultaneous rate equations that describe the population densities at energy-resolved states. In the model, we divide the electron distribution into 13 groups specified by integer j (≥ 1) with energies $E_j = (j - \frac{1}{2})\hbar\omega_{LO}$, based on the nascent electron distribution shown in Fig. 5. The temporal change in the population density N_j at the state with energy E_j ($1 < j < 13$) under the LO-phonon-induced transitions can be described by the following rate equation:

$$\frac{dN_j}{dt} = \xi_j g(t) - N_j [d + (W_{em}^j + W_{abs}^j)] + N_{j-1} W_{abs}^{j-1} + N_{j+1} (d + W_{em}^{j+1}), \quad (8)$$

where ξ_j is the population amplitude of N_j induced by a pump pulse, $g(t)$ the temporal function of electron injection, and W_{em}^j (W_{abs}^j) the rate of LO phonon emission (absorption) at energy E_j given by $W_0 F_{em}^j(E_j)$ [$W_0 F_{abs}^j(E_j)$] in Eqs. (3)–(5). The quantity d in Eq. (8) stands for an additional rate of downward population transfer from the state E_j to the state

E_{j-1} , which is added to examine possible effects on energy relaxation by other mechanisms, like the e-h interaction, when necessary. The second term on the right-hand side of Eq. (8) represents the population loss at the state with E_j , the third term the population gain from the state with E_{j-1} , and the fourth term the population gain from the state with E_{j+1} .

We choose the state with E_{13} ($E_{ex} = 12.5\hbar\omega_{LO} = 0.5375$ eV) as the highest energy level, to which no direct population by laser excitation is induced. For the state with E_{13} ,

$$\frac{dN_{13}}{dt} = -N_{13}(d + W_{em}^{13}) + N_{12}W_{abs}^{12}. \quad (9)$$

Additionally, we identify the state with E_1 ($j = 1$, $E_{ex} = 0.5\hbar\omega_{LO}$) as the lowest energy level in the model. As the state with E_1 has E_{ex} smaller than $\hbar\omega_{LO}$, no LO phonon emissions are possible, and acoustic-phonon processes become important. However, the precise description of the energy-relaxation process of N_1 needs extensive knowledge of nonequilibrium dynamics of acoustic phonons, which is beyond the present scope. Here, we simply approximate that the population at the state with E_1 can communicate with that at the state with E_2 via LO phonon absorption and emission transitions:

$$\frac{dN_1}{dt} = \xi_1 g(t) - N_1 W_{abs}^1 + N_2(d + W_{em}^2). \quad (10)$$

The magnitude of ξ_j is the only parameter in the simulation, as the magnitudes of W_{em}^j and W_{abs}^j are determined already using Eqs. (3)–(5). However, the magnitude of ξ_j is determined almost uniquely as the calculated amplitude of N_j at $\Delta t = 20$ fs has to fit to the experimental result of the nascent photoinjected electron distribution at $\Delta t = 20$ fs shown in Fig. 5. The green circles in the figure show the results of N_j at $\Delta t = 20$ fs in the simulation. The $n(\omega_{LO})$ is an important parameter that determines the magnitudes of LO phonon emission/absorption rates. It has been emphasized that the electron relaxation takes place under nonequilibrium LO phonon distributions [39,40]. However, here, we use the thermal equilibrium value of $n(\omega_{LO}) = 0.223$ for $\hbar\omega_{LO}$ at 293 K for simplicity. As seen in Eqs. (8)–(10), the model does not include any effects of density loss from the CB; the electrons injected by photoexcitation at the states with different E_j are relaxed to the lowest energy ensemble with conserving the total density constant. The simultaneous rate equations for N_j ($j = 1$ –13) were solved numerically using pump-pulse width of 75 fs, and the calculated results were convolved with respect to the probe-pulse width of 80 fs to have better comparison with experimental results.

It is true that the rate equation model introduced above is too simple to describe the relaxation processes of energetic electrons fully. The model does not include any other interactions and effects which play important roles in carrier relaxation, like effects of screening of electron–LO-phonon interaction, hot-phonon effects of electron-energy relaxation, and electron-acoustic phonon interactions [8–10,39–41]. Furthermore, the e-e interaction is treated just as the source of quasimomentum equilibration during relaxation. Nevertheless, it is very instructive to examine possible effects of the population-transfer cascade induced by LO phonon transitions on the decay dynamics of energy-resolved electron popula-

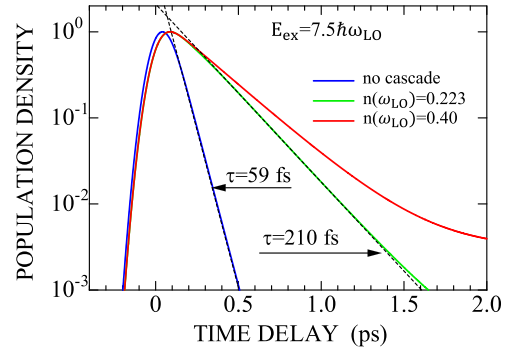


FIG. 6. Typical effects of population-transfer cascade on the temporal changes in the energy-resolved population densities in InP. Simulated population decays of the state with $E_{ex} = 7.5 \hbar\omega_{LO}$ are plotted for the case with no population-transfer cascade, blue, and under population-transfer cascade with longitudinal optical (LO) phonon occupation number of 0.223 (0.40), green (red). The broken lines on blue and green curves are the exponential-decay fits with time constants indicated in the figure.

tions in semiconductors excited with an ultrashort laser pulse, the importance of which has been pointed out for the carrier dynamics in Si [42].

Before the comparison of simulated results of the dynamics of $\rho_e(E_{ex}, \Delta t)$ with the experimental results of $\rho_e(E_{ex}, \Delta t)$, we point out typical effects of the population-transfer cascade on the dynamics of $\rho_e(E_{ex}, \Delta t)$ revealed by the simulation. As stated above, the population n_k at the initial state with e_k in the ideal theoretical frame decays with the time constant $\tau_k = 1/(W_{em} + W_{abs})$. At $E_{ex} = 7.5\hbar\omega_{LO}$ ($= 0.3225$ eV), which corresponds to the maximum of the nascent electron distribution, $\tau_k = 59.3$ fs for $n(\omega_{LO}) = 0.223$. The simulated decay profile in this case is shown by the blue curve in Fig. 6. In the simulation including the population-transfer cascade, the state E_8 ($E_{ex} = 7.5\hbar\omega_{LO}$) has four high-lying states with finite ξ_j ($j = 9$ –12). The green curve shows the simulated population decay of the state with E_8 under the population-transfer cascade with $n(\omega_{LO}) = 0.223$. The pattern of population decay changes significantly, and the decay is well approximated by an exponential decay with the time constant of 210 fs, which is 3.5 times longer than τ_k . The red curve in Fig. 6 is the simulation of the E_8 state population decay in the case of $n(\omega_{LO}) = 0.4$, which corresponds to the phonon occupation number at 400 K. Because of relatively enhanced rates of phonon-absorption processes, the population decay time becomes longer than that at $n(\omega_{LO}) = 0.223$. When the hot-phonon effect on electron relaxation is significant, $n(\omega_{LO})$ would become more enhanced, resulting in slower decay of energy-resolved populations. Therefore, the effects of the population-transfer cascade on the dynamics of $\rho_e(E_{ex}, \Delta t)$ are substantial to modify the decay time strongly.

The simulated results of the dynamics of energy-resolved populations (N_j) under the population-transfer cascade with $d = 0$, which represents the dynamics caused by the LO phonon emission and absorption transitions only, are displayed in Fig. 7(a). Here, N_j at the state with E_j is plotted on a semilogarithmic scale, and the line color specifies E_j (in units of $\hbar\omega_{LO}$) as defined in the inset of Fig. 7(c). In this

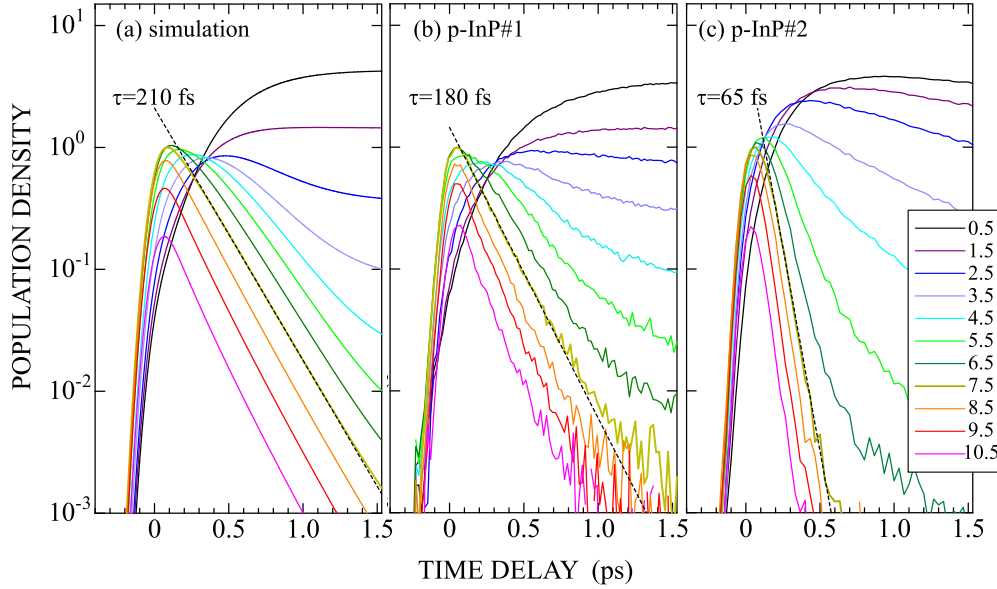


FIG. 7. Temporal changes of energy-resolved population densities in (a) simulation, (b) p -InP#1, and (c) p -InP#2. The population density at the state with E_{ex} is plotted on a semilogarithmic scale. The E_{ex} for a state is specified by different color and the magnitude of E_{ex} (given in unit of $\hbar\omega_{LO}$) shown in the inset of (c). The maximum values of the densities at the states with $E_{ex} = 7.5\hbar\omega_{LO}$ are normalized to unity. The broken lines in the figures are the exponential-decay fit to the densities at $E_{ex} = 7.5\hbar\omega_{LO}$. In the simulation, the same material constants listed in the caption of Fig. 5 were used.

figure, panels (b) and (c) show the experimentally determined $\rho_e(E_{ex}, \Delta t)$ in p -InP#1 and p -InP#2 by the methods described below.

As shown in Fig. 1(e), the quasi-equilibration in momentum space at a given E_{ex} is established with ultrafast rates < 100 fs. In such a case, it is possible to evaluate the $\rho_e(E_{ex}, \Delta t)$ from the results of time- and energy-resolved photoemission intensities (see Appendixes A and B for details). Considering a finite energy resolution in this paper, we first evaluated the angle-integrated photoemission intensity $I_{(\theta)}(E_{ex}, \Delta t)$ at a given E_{ex} with ± 21.5 meV width and transferred it to $\rho_e(E_{ex}, \Delta t)$ by correcting both the matrix-element effects and the k -dependent detection-efficiency effects of photoemission. The transformation from $I_{(\theta)}(E_{ex}, \Delta t)$ to $\rho_e(E_{ex}, \Delta t)$ is important for comparing the experimental results with theoretical simulations, as the simulation has been made for the energy-resolved electron density in the CB. The energy width for intensity integration (43 meV), which is equal to $\hbar\omega_{LO}$, is a little narrower than the energy resolution in this paper. However, we use the width to compare the experimental result directly with those of the model simulation of the population-transfer cascade by LO-phonon-induced transitions.

The results of $\rho_e(E_{ex}, \Delta t)$ in p -InP#1 (p -InP#2) are shown in Fig. 7(b) [Fig. 7(c)]. In these figures, the line color specifies E_{ex} (in units of $\hbar\omega_{LO}$) as indicated in the inset of Fig. 7(c). For both samples, and for the simulation results in Fig. 7(a), the maximum of $\rho_e(E_{ex}, \Delta t)$ at $E_{ex} = 7.5\hbar\omega_{LO}$ ($= 0.3225$ eV) is normalized to unity. In Fig. 7(b), the temporal evolutions of $\rho_e(E_{ex}, \Delta t)$ in p -InP#1 show the following three characteristics: (1) $\rho_e(E_{ex}, \Delta t)$ of the states with $E_{ex} \geq 7.5\hbar\omega_{LO}$ decay exponentially with time constants < 180 fs after their generation by laser pulses, (2) $\rho_e(E_{ex}, \Delta t)$ near the CBM ($E_{ex} < 2.5\hbar\omega_{LO}$) increases monotonically at $\Delta t < \sim 1$ ps to

the peak ~ 1.5 ps, and (3) $\rho_e(E_{ex}, \Delta t)$ of the states with E_{ex} from $2.5\hbar\omega_{LO}$ to $7.5\hbar\omega_{LO}$ show the maxima at $\Delta t < 0.5$ ps and follow complicated decay kinetics at $\Delta t > 0.5$ ps.

The simulation results for the temporal changes of $\rho_e(E_{ex}, \Delta t)$ shown in Fig. 7(a) reproduce well the characteristic features of experimentally observed results in p -InP#1. The agreement is even at quantitative levels at some points. The decay of populations at $E_{ex} = 7.5\hbar\omega_{LO}$ is fit by an exponential decay with the time constant of 210 fs in the simulation, which is longer than the experimental result (180 fs) by only 17%. The beautiful reproduction of experimental results of temporal changes in $\rho_e(E_{ex}, \Delta t)$ by the model simulation supports strongly that the Fröhlich interaction is the dominant mechanism which governs relaxation processes of photoinjected electrons in p -InP#1.

On the other hand, characteristics of decay profiles of energy-resolved population in p -InP#2 show significant differences from those of simulated results. First, $\rho_e(E_{ex}, \Delta t)$ at states near the CBM with $E_{ex} < 2.5\hbar\omega_{LO}$ decays faster than the model simulations. As shown in Appendix B, the initial electron density photoinjected in p -InP#2 starts to decrease at $\Delta t > 0.5$ ps, which is not the case in p -InP#1. Since no mechanisms of total electron-density reduction are included in the model simulation, the disagreements between the simulation and experimental results may be expected for the samples which show the loss of total electron density. Therefore, we do not go into the details of the disagreement at $\Delta t > 0.5$ ps. Second, the decay rates of $\rho_e(E_{ex}, \Delta t)$ at the states with $E_{ex} > 7.5\hbar\omega_{LO}$ in p -InP#2 are substantially higher than those in the model simulation. At $E_{ex} = 7.5\hbar\omega_{LO}$, the population decays with a time constant as short as 65 fs, while it is 210 fs in the simulation (and it is 180 fs in p -InP#1). We cannot ascribe the high decay rate in p -InP#2 to the ultrafast loss of total electron density at the timeframe of

$\Delta t < 0.4$ ps, as the density is roughly constant in p -InP#2 (see Appendix B). It is most likely that other mechanisms, together with the Fröhlich interaction, contribute strongly to the decay rates of populations at high E_{ex} states in p -InP#2. The simultaneous rate equations introduced above predict that the population decay time at the state with $E_{ex} = 7.5\hbar\omega_{LO}$ becomes 65 fs when we introduce additionally $d = 18 \times 10^{12} \text{ s}^{-1}$ in Eq. (8). The additional rate corresponds to $-dE_{ex}/dt = 0.77 \text{ eV/ps}$, larger than the rate by the Fröhlich interaction. We presume that the additional rate of downward population transfer in p -InP#2 is due to the e-h interaction.

The effects of e-h interactions and of acceptor doping on the energy-relaxation rate of energetic electrons in GaAs and InP have been studied in detail using Monte Carlo simulations [10,41]. The efficient energy loss from the electron subsystem by the e-h interaction originates from the high efficiency of hole-phonon scattering through the unscreened deformation-potential interaction [41]. As the rate of e-h scattering is proportional to the hole concentration, the role of the e-h interaction on the electron-energy loss is more significant in p -InP#2 than in p -InP#1; the doping level in p -InP#2 is higher than that in p -InP#1 by more than a factor 10, even if the photoinjected hole concentration is included. Furthermore, the important role of electron-acceptor collisions in the electronic energy loss has been shown [10]. These channels, characteristic of the heavily doped samples, can contribute to the electron energy-relaxation rate, together with the Fröhlich interaction, in p -InP#2.

C. Specific internal structure of electron ensemble for quasithermalization

As shown above, the quasithermalization of photoinjected electrons in the Γ valley in p -InP is established at the specific distribution of the energetic-electron ensemble, despite significant differences in the nascent energetic-electron distributions and in the energy-relaxation rates for nonthermal electrons. The difference in the time delays to establish the quasithermalization reflects how fast the distribution ideal for quasithermalization is formed. At the specific electron distribution, photoinjected electrons with $\rho_0 \approx 1.0 \times 10^{17} \text{ cm}^{-3}$ are confined in the CB states below $E_{ex} = 0.27 \text{ eV}$ with wave vectors $< 0.09 \text{ \AA}^{-1}$. The electronic structure of the Γ valley of CB in InP is well described as a nonparabolic spherical band characterized by $m^* = 0.080m_e$ and $a = 0.596 \text{ eV}^{-1}$ [25]. For this band, the number of states N_s included below $E_{ex} = 0.27 \text{ eV}$ is $N_s = 1.83 \times 10^{19} \text{ cm}^{-3}$. Then the specific electronic distribution for quasithermalization can be characterized by the occupation ratio $\gamma = 7.7 \times 10^{-3}$; γ is defined as $\gamma = \rho_0/N_s$.

The conclusions obtained for p -InP in this paper are essentially the same as those obtained for p -GaAs in our previous study [18]. In both GaAs and InP, the quasithermalization of photoinjected electrons in the Γ valley is established only after a substantial amount of energy stored in the electron subsystem is transferred into other subsystems. Quantitatively, however, there are some differences in the quasithermalization processes in GaAs and InP. Under similar excitation density of $\sim 1 \times 10^{17} \text{ cm}^{-3}$ in p -type samples with similar magnitudes of $h_0 = 1 \times 10^{17} \text{ cm}^{-3}$, it takes 600 fs to establish

quasithermalization in p -GaAs [18], while it is 420 fs in p -InP. In this paper, we have shown that the time delays for quasithermalization become shorter in samples with higher energy-relaxation rates. When we consider that the energy-relaxation rate by the Fröhlich interaction in InP is higher than that in GaAs, the observed difference in time for establishing quasithermalization can be consistent with our general conclusion that the quasithermalization is achieved when a substantial amount of energy stored in the electron subsystem is transferred to other subsystems.

The rate of e-e scattering, which is the most important interaction to establish electronic quasithermalization, depends not only on the density in the real space but also on the distribution in the momentum space [3,9,10,41]. Our results show that the energy exchange among photoinjected electrons by the e-e interaction is not efficient enough to establish the detailed balance necessary for electronic thermalization for the photoinjected nascent electron distributions in a short timeframe < 100 fs. Instead, the system evolves in such a way that a substantial part of the energy stored in the electron subsystem is dissipated to other subsystems via the e-ph and e-h interactions to condense nonthermal electrons into a specific phase space characterized by the critical excess energy E_c and critical wave vector k_c . The magnitudes of E_c and k_c are excitation density dependent [18]. Under the excitation density of $\sim 1 \times 10^{17} \text{ cm}^{-3}$, we find that $E_c = 0.27 \text{ eV}$ and $k_c = 0.09 \text{ \AA}^{-1}$ in p -InP in this paper, while $E_c = 0.14 \text{ eV}$ and $k_c = 0.04 \text{ \AA}^{-1}$ in p -GaAs [18].

The energy exchange among nonthermal electrons, the distribution of which is far from equilibrium, takes place mainly via binary collisions under a screened Coulomb interaction. In this situation, the energy exchange among the hot carriers is quite ineffective [19]. It is highly desirable to further study the energy-exchange processes using sophisticated theoretical methods to make the physical meaning of the magnitudes of these parameters clear and to understand thoroughly the carrier relaxation processes in semiconductors. We leave it as an important future issue and emphasize here that the delayed quasithermalization of the electron subsystem in the Γ valley relaxation, discovered in GaAs in Ref. [18], is not specific to GaAs, but it is more general in other direct-gap semiconductors. In fact, the delayed quasithermalization of photoinjected energetic electrons in the Γ valley has been observed in CdTe, a prototypical II-VI semiconductor [43].

V. SUMMARY

We have studied ultrafast scattering dynamics of photoinjected electrons at the nonthermal regime of the Γ -valley relaxation in p -InP, based on the time-, energy-, and momentum-resolved electron distribution functions obtained by TR-ARPES. In p -InP, the quasithermalization of photoinjected electrons is established when the electron ensemble is relaxed into the specific electron distribution during relaxation at a finite time delay of several hundreds of femtoseconds. For an electron density of $\sim 1 \times 10^{17} \text{ cm}^{-3}$, the electron distribution ideal for the quasithermalization is characterized by the condensation in the phase space with the energy $< 0.27 \text{ eV}$ and with wave vectors $< 0.09 \text{ \AA}^{-1}$. Finite time delays for the quasithermalization can be regarded as the formation time of this

specific distribution, starting from the photoinjected nascent electron distributions, controlled by the energy-relaxation rates in the samples. The conclusions obtained for *p*-InP are essentially the same as those observed for *p*-GaAs in our previous study [18]. Therefore, the characteristic feature of Γ -valley relaxation that the nonthermal regime lasts for several hundreds of femtoseconds of excitation is not specific to GaAs but is more general in direct-gap semiconductors.

Intra- Γ -valley relaxations of energetic electrons in semiconductors with E_G wider than the highest E_{ex} can be regarded as the simplest process of energetic carrier relaxations in semiconductors; the complicated processes of intervalley scatterings and impact-ionization processes are not involved. However, it is still complicated, as the e-ph, e-h, and e-e interactions act competitively and/or cooperatively. Our results show that the energy exchange among photoinjected electrons by the e-e interaction is not efficient enough to achieve the detailed balance necessary for electronic thermalization for the photoinjected nascent electron distributions in a short timeframe <100 fs. Instead, the system evolves in such a way that a substantial part of the energy in the electron subsystem is dissipated to other subsystems via the e-ph and e-h interactions until the electron distributions ideal for the quasithermalization are prepared.

The internal structure of the electron ensemble ideal for the quasithermalization in *p*-InP revealed in this paper is not the same as that in *p*-GaAs; γ ($= 7.7 \times 10^{-3}$) in *p*-InP is smaller than that (1.3×10^{-2}) in *p*-GaAs, and the electron temperature (800 K in InP) when quasithermalization is established is higher than that (600 K) in GaAs under excitation generating nascent electron distributions with similar ρ_0 and \bar{E}_m . How these parameters are dependent on the energy-exchange rate by e-e interaction, energy-relaxation rate by the Fröhlich interaction, excitation density, and other interactions are important future issues to thoroughly understand the carrier relaxation processes in semiconductors.

ACKNOWLEDGMENT

This paper was supported by Japan Society for the Promotion of Science KAKENHI Grants No. 24000006 and No. 19H01826.

APPENDIX A: MATRIX-ELEMENT EFFECTS ON THE LOW-ENERGY PHOTOEMISSION FROM InP(110)-(1 \times 1)

The photoemission process inherently involves an interplay between the bulk and surface phenomena. In terms of the three-step model on photoemission, the process is subdivided into three independent and sequential steps: (i) optical excitation of the electron in the bulk, (ii) travel of the excited electron to the surface, and (iii) escape of the photoelectron into vacuum. The photoemission intensity $I_e(k, E_K, \Delta t)$ is then governed by the photoemission efficiency $\eta_e(k, E_K)$, which includes all effects of the following three independent terms: the optical-transition probability in step (i), the scattering probability for the traveling electrons in step (ii), and the transmission probability through the surface potential barrier in step (iii) [16,17]. Because of the k - and E -dependent $\eta_e(k, E_K)$, $I_e(k, E_K, \Delta t)$ does not correctly rep-

resent the electron-distribution function $f_e(k, E, \Delta t)$ of the initial state in step (i) in many cases. Therefore, an understanding of this difference, the so-called matrix-element effect, is crucial for determining $f_e(k, E, \Delta t)$ from ARPES spectra.

In this paper, the photoemission takes place at the energy range of 5.8–7.0 eV above the valence band maximum (VBM), which is ~ 1 eV above the vacuum level of InP. Despite extensive experimental and theoretical studies to make clear several characteristics of the matrix-element effects in the photoemission from semiconductor surfaces [44–47], a clear characterization of the effects at such a very low-energy region has not been established. To make clear the matrix-element effect at this energy region of InP with well-ordered (110) surfaces, we study $\eta_e(k, E_K)$ in the photoemission process from a given electron distribution in the Γ valley. We used an *n*-type InP sample (purchased from Showa Denko K. K.), which includes a carrier concentration of $4.5 \times 10^{18} \text{ cm}^{-3}$ with the thermalized electron distribution $N_e(E_{ex} : E_F, T_e)$ near the CBM, where E_{ex} is the excess energy measured from the CBM, E_F is the Fermi level, and T_e is the electron temperature. The photoemission $I_e(k, E_K)$ from the thermalized electron ensemble was measured by a tunable probe light with $h\nu_{\text{probe}}$ ranging from 4.65 to 5.17 eV. By examining the correlations between $I_e(k, E_K)$ and $N_e(E_{ex} : E_F, T_e)$, we can gain deeper insight into the matrix-element effect. The third harmonics of fundamental output from a 76 MHz Ti-sapphire laser, generating 75 fs laser pulses centered at photon energies from 1.55 to 1.72 eV, were used as probe-light pulses. The fluences of the probe pulses with different $h\nu_{\text{probe}}$ were kept constant (1.5×10^{10} photons/cm²) within $\pm 5\%$ of fluctuation.

1. The determination of E_K for photoelectrons emitted from n-InP

In the photoemission process in semiconductors, the initial state characterized by the one-electron energy level $E_i(\vec{k})$ at a wave vector \vec{k} , referenced to the VBM, is excited to the state above the vacuum level by the probe light with photon energy $h\nu_{\text{probe}}$ and then ionized. As the Fermi levels of the analyzer and InP bulk match, the energy E_{mes} of a photoelectron measured by the analyzer with the work function W_{ana} is referenced to the energy $E_F + W_{ana}$ above the VBM. On the other hand, the kinetic energy E_K of a photoelectron is referenced to the vacuum level of a sample, which is specified by the ionization energy Φ_{vac} from the VBM. Then

$$E_K(\vec{k}) = h\nu_{\text{probe}} + E_i(\vec{k}) - \Phi_{\text{vac}}. \quad (\text{A1})$$

In the photoemission process, the parallel component of momentum (k_{\parallel}) is conserved, and k_{\parallel} is determined by the relation:

$$k_{\parallel} = \frac{1}{\hbar} \sqrt{2m_e E_K} \sin\theta, \quad (\text{A2})$$

where \hbar is Planck's constant, and θ is the emission angle with respect to the surface normal [28]. Here, k_{\parallel} and E_K are two important quantities that characterize the photoemission.

For determining E_K , it is most straightforward and reliable to experimentally measure the low-energy cutoff energy $E_{L\text{ow}}$

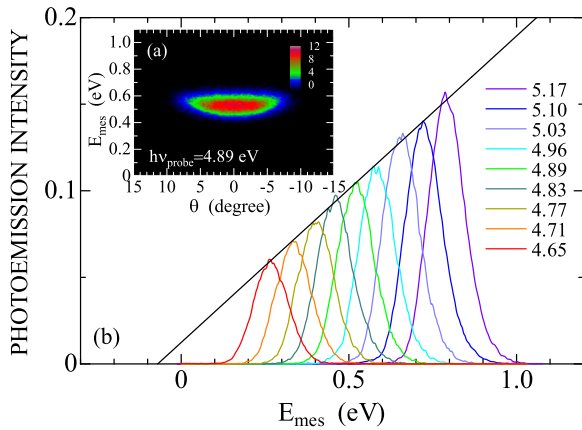


FIG. 8. (a) A photoemission image probed by 4.89 eV light for n -InP. Photoemission intensities specified by the color scale are plotted as a function of emission angle (θ) and E_{mes} . (b) The spectra of normal photoemission as a function of E_{mes} measured for n -InP, using probe-light pulses with different $h\nu_{probe}$ ranging from 4.65 to 5.17 eV. The black line shows the least-square fit to the peak intensities of respective spectra.

of the photoemission, which corresponds to the vacuum level of the sample at energy Φ_{vac} [30]. However, the experimental determination needs higher Φ_{vac} than $E_F + W_{ana}$. In our detection system, $W_{ana} = 4.337$ eV. For p -doped samples, where E_F is $< \sim 0.5$ eV above the VBM, we can directly determine the magnitude of E_{Low} and hence E_K experimentally. In view of Eq. (A1), E_K of photoelectrons emitted from the CBM, $E_K(\text{CBM})$, is

$$E_K(\text{CBM}) = E_G + h\nu_{probe} - \Phi_{vac}. \quad (\text{A3})$$

Our experimental results of $E_K(\text{CBM})$ and $h\nu_{probe}$ for p -InP samples, together with $E_G = 1.353$ eV at 293 K [26], have given $\Phi_{vac} = 5.74 \pm 0.01$ eV. The magnitude of Φ_{vac} agrees reasonably well with those reported previously [27].

On the other hand, Fermi levels of highly n -doped InP samples are located above the CBM. The sample used here includes electrons of $4.5 \times 10^{18} \text{ cm}^{-3}$, which corresponds to E_F above the CBM by 0.11 eV (1.463 eV above the VBM). It is estimated that E_{Low} is at negative range of E_{mes} measured by our analyzer; E_{Low} cannot be determined experimentally. Therefore, we need some analyses to determine E_K for photoemitted electrons from n -InP, based on the results of the photoemission spectra as a function of $h\nu_{probe}$.

In Fig. 8(a), we show a typical example of the photoemission images detected by the present measurements; the photoemission intensities, specified by the color scale, are plotted as a function of θ and E_{mes} . To determine E_K , we first analyze the normal photoemission spectra, as they represent selectively the electron distributions along the Γ - K line [see Fig. 1(c)]. The normal photoemission spectra probed by several $h\nu_{probe}$, obtained by integrating photoemission intensities within emission angles $\pm 0.5^\circ$, are plotted as a function of E_{mes} in Fig. 8(b). The peak energy of photoemission increases with increasing $h\nu_{probe}$. At the same time, the intensities of photoemission increase with increasing $h\nu_{probe}$, irrespective of the constant fluences of the probe pulses with different $h\nu_{probe}$. The peak intensity of the photoemission spectrum

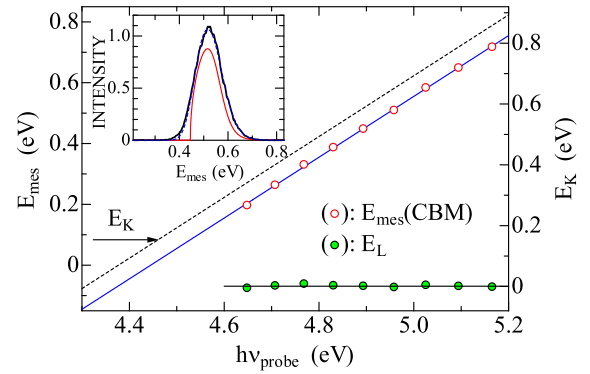


FIG. 9. The energy $E_{mes}(\text{CBM})$ of photoemission from the conduction band minimum (CBM) in the measured photoemission spectrum, red circles, as a function of $h\nu_{probe}$. The broken line shows the $E_K(\text{CBM})$ predicted from the experimental result of $\Phi_{vac} = 5.74$ eV. The difference $E_{mes}(\text{CBM}) - E_K(\text{CBM})$ is plotted by the green circles. In the inset, the black curve is the normal photoemission spectrum by 4.89 eV probe light, for which possible distortions in spectral shape coming from energy-dependent intensity enhancements is corrected. The red curve shows the calculated electron distribution function in n -InP, and the broken blue curve is the function convolved with respect to the energy resolution of 55 meV. They are plotted with an offset Δ in energy to match the peak energy with the experimental black curve.

at a given $h\nu_{probe}$ is described well by the linear function (black straight line) which intersects with the abscissa at $E_{mes} = -0.070 \pm 0.002$ eV. The result shows clearly that the efficiency of generating photoelectrons increases linearly with the final-state energy reached by optical transitions from the common initial $N_e(E_{ex}; E_F, T_e)$ in step (i). This effect reflects one of the important matrix-element effects in the present case. We discuss this feature quantitatively later, but here, we pay attention to the fact that the effect possibly distorts the spectral line shape of photoemission from the initial electron distribution.

To minimize the distortions in spectral line shapes, we first correct this effect by dividing the spectra by the linear function shown in Fig. 8(b) and analyze the corrected spectra to determine the energy $E_{mes}(\text{CBM})$ at which the photoemissions from the CBM are detected in the spectra. The solid black curve in the inset of Fig. 9 is the corrected normal photoemission spectrum for $h\nu_{probe} = 4.89$ eV. The red curve is the thermalized electron distribution function $N_e(E_{ex}; E_F, T_e)$ at the CB of InP, characterized by an effective mass of $0.080m_e$ and the first-order nonparabolic factor of 0.596 [25]. The result calculated with $E_F = 0.11$ eV and $T_e = 293$ K is plotted with a given offset Δ of energy. The energy of the distribution peak is higher than the CBM by 71 meV. The broken blue curve is the distribution function convolved with respect to a finite energy resolution of 55 meV. The function with $\Delta = 0.445$ eV describes reasonably well the corrected photoemission spectrum. The analysis allows us to determine the $E_{mes}(\text{CBM})$ in the photoemission spectrum measured by a given $h\nu_{probe}$.

The red circles in Fig. 9 show the $E_{mes}(\text{CBM})$ as a function of $h\nu_{probe}$ ranging from 4.53 to 5.25 eV; a linear relation is evident. However, the magnitude of $E_{mes}(\text{CBM})$ is lower than

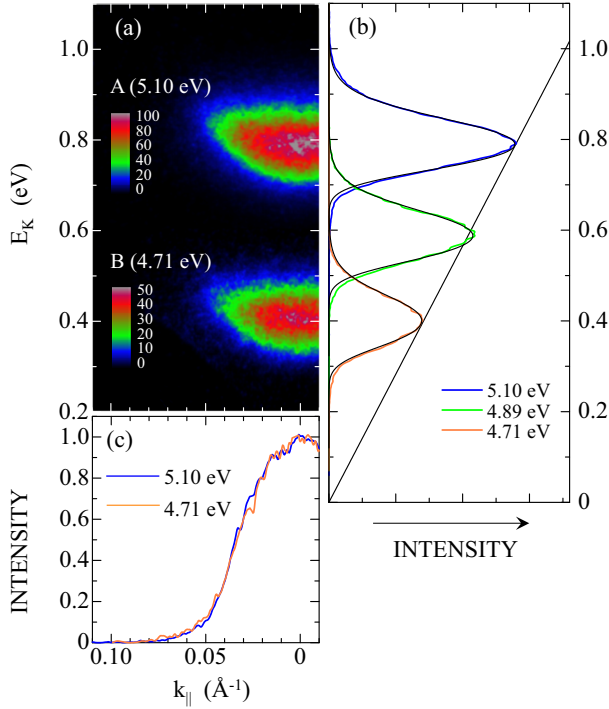


FIG. 10. (a) Images of photoemission from n -InP. Photoemission intensities, specified by the color scales, are plotted as a function of E_K and k_{\parallel} . Image labeled A was probed at $h\nu_{\text{probe}} = 5.10$ eV, while image B was probed at $h\nu_{\text{probe}} = 4.71$ eV. Note that the amplitudes of color scales are different. (b) The normal photoemission spectra, determined by integrating photoemission intensities at $k_{\parallel} = 0 \pm 0.005$ Å, for images A and B, together with the spectrum probed at $h\nu_{\text{probe}} = 4.89$ eV. The solid black curves are the simulated photoemission spectra (see the text). (c) The momentum-resolved intensities at the peak energies of images A and B. The intensities are normalized with respect to the intensities at $k_{\parallel} = 0$ Å⁻¹.

$E_K(\text{CBM})$ expected from Eq. (A3) with the experimentally determined $\Phi_{\text{vac}} = 5.74 \pm 0.01$ eV. The difference, shown by green circles, is -0.070 eV on average, indicating that $E_{\text{Low}} = -0.070$ eV on the scale of E_{mes} ; $E_K = E_{\text{mes}} + 0.070$ eV. The electron concentration of 4.5×10^{18} cm⁻³ in our n -InP sample implies that E_F is 0.11 eV higher than E_G ($E_F = 1.463$ eV above the VBM). Therefore, $E_{\text{mes}} = 0$, corresponds the energy level of 5.81 eV above the VBM. In view of our experimental value $\Phi_{\text{vac}} = 5.74$ eV, the estimated magnitude of E_{Low} is totally consistent. We adopt hereafter our conclusion that $E_K = E_{\text{mes}} + 0.070$ eV for analyzing the matrix-element effect of photoemission in our n -InP crystal.

2. Characteristics of the matrix-element effect on photoemission from InP with (110)-(1 × 1) surfaces

Figure 10(a) shows the energy- and momentum-resolved (k -resolved) maps of photoemissions from n -InP probed by $h\nu_{\text{probe}} = 5.10$ eV, image A, and by $h\nu_{\text{probe}} = 4.71$ eV, image B. In the figure, photoemission intensities specified by color scales are plotted as a function of k_{\parallel} and the kinetic energy E_K of photoelectrons. The spectra of normal photoemission $I_e(\bar{\Gamma}, E_K)$, which are now obtained by integrating photoemission intensities for the range of $k_{\parallel} = 0 \pm 0.005$ Å⁻¹, are

displayed in Fig. 9(b), together with the spectrum obtained by $h\nu_{\text{probe}} = 4.89$ eV. The difference in the peak energies of images A and B is 0.44 eV, which is identical to the difference in $h\nu_{\text{probe}}$ for probing peaks A and B.

In the measurements, the [110] crystal axis is aligned along the surface normal (z), and the x and y axes correspond to the [001] and $[1\bar{1}0]$ directions. Under this geometry, the BBZ and SBZ have the relation shown in Fig. 1(c) [28]. As described in the main text, the spectra of normal photoemissions reflect the electron distributions along the Γ - K line of the BBZ. On the other hand, the off-normal photoemission at a given k_{\parallel} is a superposition of many contributions from such states that are projected on the one-dimensional cut along the $\bar{\Gamma}$ - \bar{Y} direction of the SBZ.

In Fig. 10(c), the momentum-resolved intensities at the peak energies for images A and B are compared; the distributions do not depend on $h\nu_{\text{probe}}$. Therefore, there are no significant matrix-element effects on the momentum-resolved characteristics in the photoemission processes. On the other hand, as seen in Figs. 8, 10(a), and 10(b), the intensities of photoemission from the common thermalized electron distribution with the same density are enhanced at higher probe-photon energies; electrons excited to higher energy in step (i) of the three-step model show larger $I_e(\bar{\Gamma}, E_K)$. The solid black line in Fig. 10(b) represents the least square fit to the intensities at the maxima of the spectra measured at different $h\nu_{\text{probe}}$; the line crosses the abscissa at $E_K = 0$. The result shows that the $I_e(\bar{\Gamma}, E_K)$ is represented by

$$I_e(\bar{\Gamma}, E_K) = \sigma E_K f_e^*(\bar{\Gamma}, E_K), \quad (\text{A4})$$

where σ is a constant and $f_e^*(\bar{\Gamma}, E_K)$ stands for the electron distribution at the final state of the optical excitation of step (i), reached by the vertical transitions from the electron distribution $N_e(E_{\text{ex}}; E_F, T_e)$ under the relation $E_K = E_{\text{ex}} + h\nu_{\text{probe}} - \chi$.

We examine more closely the relation given by Eq. (A4) by simulating the $I_e(\bar{\Gamma}, E_K)$ using the initial electron distribution function $N_e(E_{\text{ex}}; E_F, T_e)$ near the CBM at $T = 293$ K. When we assume that the optical excitation in step (i) brings the $N_e(E_{\text{ex}}; E_F, T_e)$ up to the final-state energy region without changing the energy-distribution characteristics,

$$\begin{aligned} f_e^*(\bar{\Gamma}, E_K) &= N_e(\varepsilon; E_F, T_e) \quad \text{for } \varepsilon \geq 0, \\ f_e^*(\bar{\Gamma}, E_K) &= 0 \quad \text{for } \varepsilon < 0, \end{aligned} \quad (\text{A5})$$

where $\varepsilon = E_K - (h\nu_{\text{probe}} - \chi)$. The photoemission spectra were calculated using the relation given by Eq. (A4), and they were convolved with respect to a finite energy resolution of 55 meV. The black curves in Fig. 10(b) show the calculated results. The simulation reproduces the experimental results reasonably well [48,49], substantiating the empirical relation between the photoemission spectra and the electron distribution functions given by Eq. (A4).

As described above, the main feature of the matrix-element effects on the normal photoemission spectra in the present experiments is the E_K -dependent photoemission intensity, which can be characterized by Eq.(A4). Although a thorough understanding of the matrix-element effects of very low-energy photoemission, just ~ 1 eV above the vacuum level, needs more expensive experimental and theoretical studies, we leave

it as an important future issue. In this paper, we use Eq. (A4) to determine the time-resolved electron distribution functions during relaxation. We comment here that the empirical rule of Eq. (A4) was also obtained recently for GaAs with (110) surfaces [18], which have structural and electronic properties like those of InP [27]. From the results shown in Figs. 8–10, the relation given by Eq. (A4) has been proved for the energy range 1.1 eV above the vacuum level. The electron distributions are induced above the energy range but < 1.25 eV in p -InP, as discussed in the main text. We assume that the same E_K -dependent photoemission intensity holds for the energy range between 1.1 and 1.25 eV.

APPENDIX B: TEMPORAL CHANGES IN THE TOTAL ELECTRON DENSITIES IN THE THREE-DIMENSIONAL k SPACE ESTIMATED FROM THE ANGLE-INTEGRATED PHOTOEMISSION INTENSITIES

Laser-induced excitation densities ρ_0 in real space in semiconductors can be estimated by the formula described in Sec. II of the main text. However, it is not guaranteed that the initial excitation density is conserved during the whole timeframe in measuring relaxation processes in the TR-ARPES study. In the photoemission measurements, the electrons within a limited depth from the surface can be probed. Therefore, any processes that cause electron transports from the detection depth to the outer regions, like diffusion or hot-electron transports, can reduce the electron density that governs several important processes in the relaxation. The nonradiative recombination processes characteristic of the high-energy minority carriers can also be a cause of reducing the density [50–55]. As the photoemission spectroscopy is surface sensitive, the deep-level defects not only in the bulk but also on the surfaces can act as the nonradiative recombination centers. Therefore, how the electron density in the CB changes in the timeframe of measurement is an important issue for correctly interpreting the results obtained by TR-ARPES.

The photoemission intensity with E_K detected by TR-ARPES is proportional to the electron density at an initial state with E_{ex} in the CB. However, it is not trivial to determine the total electron density N_{tot} in the three-dimensional k space from the detected photoemission intensities, as the constant—which correlates the energy-resolved photoemission intensity and the electron density at the initial state responsible for the photoemission—depends on several factors. One is the matrix-element effects discussed in Appendix A. The other important factor which gives significant effects on the magnitude of the proportionality constant is the detection efficiency $\eta_d(k, E_{ex})$ specific to the method of the measurement. As shown in Fig. 1(c), we measure the photoemission image for the detection plane, which represents a one-dimensional cut, along $\bar{\Gamma}$ – \bar{Y} of the SBZ, of the two-dimensional projection of electron distributions in the three-dimensional k space. Therefore, to quantify the correlation between the measured photoemission intensities and the electron densities at the initial states, it is necessary to probe photoemission images at a whole azimuthal angle range in general cases.

In this paper on the Γ -valley relaxation of photoinjected electrons, the k space near the CBM can be approximated well

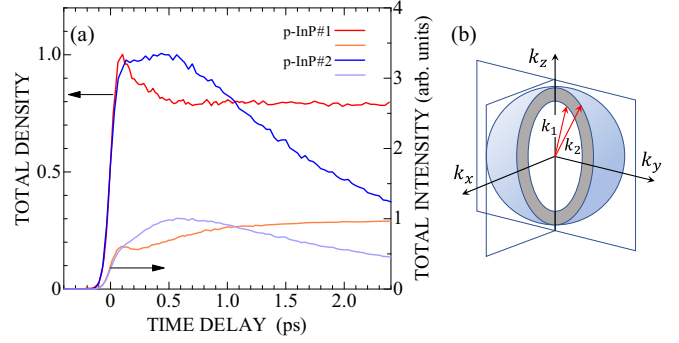


FIG. 11. (a) The estimated total electron density in the conduction band in p -InP#1, red, and p -InP#2, blue, under excitation of s -polarized 1.70 eV light at 293 K. The maximum value is normalized to unity in each sample, which corresponds to the density of $1.0 \times 10^{17} \text{ cm}^{-3}$. The orange (light blue) curve (on the right-hand scale) shows the total of angle-integrated intensities of photoemission without any corrections. (b) A schematic representation of the detection volume for evaluating the detection-efficiency factor in photoemission. The y - z plane corresponds to the detection plane for photoemission (see the text).

to be spherical (but not parabolic) for a small E_{ex} (< 0.6 eV), and the electron distribution at the states with a given E_{ex} is not dependent on k because of the ultrafast momentum equilibration by the e-e interaction. In such a case, it is possible to evaluate $\eta_d(k, E_{ex})$ which makes it possible to convert the measured photoemission intensity in the detection plane to the electron density in the three-dimensional k space, as described below.

For a spherical nonparabolic band characterized by m^* and α , we introduce the volume of the shell in k space bounded by the two surfaces on which the energy E is constant, one surface on which the energy is E_1 referenced from the CBM and the other on which the energy is E_2 ($E_2 = E_1 + \delta E > E_1$). We assume that the electron densities $\rho_e(E_i)$ are included uniformly in the volume of the shell, given by $\frac{4}{3}\pi(k_2^3 - k_1^3)$; the relation between E_i and k_i is given by

$$\frac{\hbar^2 k_i^2}{2m^*} = E_i(1 + \alpha E_i). \quad (\text{B1})$$

Then the characteristic k space volume v_0 per electron is $v_0 = \frac{4\pi}{3\rho_e(E_1)}(k_2^3 - k_1^3)$. On the other hand, the detection plane of photoelectrons is the plane which includes the origin of the k space and $\bar{\Gamma}$ [see Fig. 11(b)], and it includes the cross-section S of the shell between the E_1 and E_2 surfaces; S is given by $S = \pi(k_2^2 - k_1^2)$. Because of a finite angle resolution of the detection, the detection plane is not ideally two-dimensional. When we introduce the thickness δ for the plane, which reflects a finite angle resolution of the detection, then the detection cuboid includes a part of the shell volume given by $S\delta$. We call this volume the *detection volume* v_d ; $v_d = \pi(k_2^2 - k_1^2)\delta$. The density $n_d(E_1)$ of electrons included in the detection volume is

$$n_d(E_1) = \frac{v_d}{v_0} = \frac{3\delta(k_1 + k_2)}{4(k_1^2 + k_1k_2 + k_2^2)} \rho_e(E_1), \quad (\text{B2})$$

and the $n_d(E_1)$ determines the intensity of photoemission $I_d(E_1)$ from the detection volume characterized by E_1 and E_2 ; $I_d(E_1) \propto n_d(E_1)$ [56]. Equation (B2) shows that the $n_d(E_1)$ is a fraction of $\rho_e(E_1)$ multiplied by the detection efficiency $\eta_d(E_{ex}, k) = 3\delta(k_1 + k_2)/4(k_1^2 + k_1k_2 + k_2^2)$. Therefore, the magnitude of $\rho_e(E_1)$ at Δt , which is the energy- and time-resolved electron density $\rho_e(E_{ex}, \Delta t)$, can be estimated from $I_d(E_1)$ and $\eta_d(E_{ex}, k)$.

Although it is preferred that $\delta E (= E_2 - E_1)$ is infinitely small in precise determination of $\eta_d(E_{ex}, k)$, the energy resolution is limited to 55 ± 5 meV in the present measurement. Here, we estimate the total electron density N_{tot} in the three-dimensional k space as the sum of $\rho_e(E_{ex})$ estimated for a finite width of $\delta E = 43$ meV, which was chosen to compare the temporal changes in $\rho_e(E_{ex})$ directly with theoretical results of LO-phonon-induced transitions. We confirmed that the estimated N_{tot} with different magnitudes of δE ranging from 40 to 60 meV are essentially the same.

As described above, the photoemission intensity must be corrected, in estimating N_{tot} , with respect to two effects: one is the matrix-element effect, and the other is the detection-efficiency effect. The matrix-element effect is corrected for the photoemission intensity as a function of E_K , as described in Appendix A, while the detection-efficiency effect is characteristic of the photoemission intensity as a function of E_{ex} . Therefore, we first evaluate the angle-integrated photoemission intensity $I_{(\theta)}(\bar{E}_K, \Delta t)$ for the kinetic energy range between E_{K1} and E_{K2} at a given Δt from the E_K - and k -resolved image data [$\bar{E}_K = (E_{K1} + E_{K2})/2$], and $I_{(\theta)}(\bar{E}_K, \Delta t)$ is divided by \bar{E}_K to correct the matrix-element effect of photoemission. As $E_{ex} = E_K - E_K(\text{CBM})$, the kinetic energy range between E_{K1} and E_{K2} is transformed to the excess energy range between E_1 and E_2 of the initial states for photoemission. Then the obtained value of $I_{(\theta)}(\bar{E}_K, \Delta t)/\bar{E}_K$ is proportional to $n_d(E_1)$ for the excess energy range between E_1 and E_2 . As a next step, we correct the detection-efficiency effect to estimate $\rho_e(E_1)$ in the shell volume between E_1 and E_2 in the three-dimensional k space, using $\eta_d(E_{ex}, k)$ derived above. By summing up $\rho_e(E_1)$ for the whole energy range concerned, we can estimate the total electron density N_{tot} in the CB as a function of Δt .

As an example of estimating the total electron density N_{tot} in the CB, we describe the results under s -polarized 1.70 eV excitation for p -InP#1 and #2. The orange (p -InP#1) and light blue (p -InP#2) curves in Fig. 11 show the total of $I_{(\theta)}(\bar{E}_K, \Delta t)$ obtained for the energy range from $E_{K1} = E_K(\text{CBM}) - 0.0215$ eV to $E_{K2} = E_K(\text{CBM}) + 0.5375$ eV. Intensities at negative E_{K1} regions come from the photoemissions detected

at the negative range because of a finite energy resolution of the measurements. These curves show temporal evolutions of the total photoemission intensities emitted from the whole detection volume as a function of Δt . In p -InP#1, the intensity decreases first just after the photoexcitation partially and then increases gradually to the peak ~ 2.5 ps. In p -InP#2, the total intensity increases to the maximum around $\Delta t = 0.6$ ps after pump-light-induced rapid growth and then decreases at $\Delta t > 0.6$ ps. As the changes in the total of $I_{(\theta)}(E_K, \Delta t)$ include both matrix-element and detection-efficiency effects, they do not correctly represent the temporal changes in N_{tot} in the CB.

The red and blue curves in Fig. 11 show the estimated N_{tot} in the CB, obtained by correcting the matrix-element and detection-efficiency effects using the method described above. In p -InP#1, there is a fast decrease in N_{tot} by $\sim 20\%$ just after the excitation, but it stays constant until $\Delta t \sim 2.5$ ps. We find that the estimated N_{tot} decreases nearly exponentially with a time constant of 200 ps at longer timeframe. In p -InP#2, on the other hand, the fast decrease just after the excitation cannot be detected, and N_{tot} shows a roughly constant magnitude at $\Delta t < 0.5$ ps. It decreases with the decay time of 1.9 ps for the timeframe in Fig. 11. As to the temporal changes in N_{tot} at the first 500 fs in p -InP#2, we may need to introduce one more correction to estimate the density from the photoemission intensity. In this sample, the decay time of $I_{(\theta)}(\bar{E}_K, \Delta t)$ at $\bar{E}_K > 1.0$ eV ($E_{ex} > 6.5\hbar\omega_{\text{LO}}$) is < 65 fs, which is shorter than the temporal width of probe-light pulse (~ 80 fs). In such a situation, the relation between the photoemission intensity and the electron density at the initial state becomes complicated. However, without going into the details of this higher-order correction here, we conclude that N_{tot} changes at most 20% in the temporal frame of the first 500 fs of excitation within which the quasithermalization of photoinjected electrons is established. Therefore, the results obtained in the main text can be regarded as those induced by the processes under a roughly constant density of electrons in the Γ valley, although possible small effects of the ultrafast partial loss of the electron density cannot be excluded.

In the later timeframe after 1 ps of excitation, temporal changes in N_{tot} in the two samples are not the same, suggesting significant difference in e-h recombination processes at the hot-electron regime. The mechanisms which cause the ultrafast partial loss of N_{tot} in a few hundreds of femtoseconds of excitation and the sample-dependent rates of e-h recombination in the picosecond temporal range are not clear at this moment. We leave them as open questions to be studied in the future as interesting issues in the hot-electron and isothermal regimes of carrier relaxation processes in semiconductors.

-
- [1] C. Delerue and M. Lannoo, *Nanostructures: Theory and Modeling, Nanoscience and Technology* (Springer Verlag, Berlin, 2004).
- [2] A. Polman and H. A. Atwater, *Nat. Mater.* **11**, 174 (2012).
- [3] J. Shah, *Ultrafast Spectroscopy of Semiconductors and Semiconductor Nanostructures*, 2nd ed. (Springer, Berlin, 1999).
- [4] F. Rossi and T. Kuhn, *Rev. Mod. Phys.* **74**, 895 (2002).

- [5] V. M. Axt and T. Kuhn, *Rep. Prog. Phys.* **67**, 433 (2004) and references therein.
- [6] W. Z. Lin, R. W. Schoenlein, J. G. Fujimoto, and E. P. Ippen, *IEEE J. Quantum Electron.* **24**, 267 (1988).
- [7] A. Leitenstorfer, C. Fürst, A. Laubereau, W. Kaiser, G. Tränkle, and G. Weimann, *Phys. Rev. Lett.* **76**, 1545 (1996).
- [8] T. Elsaesser, J. Shah, L. Rota, and P. Lugli, *Phys. Rev. Lett.* **66**, 1757 (1991).

- [9] L. Rota, P. Lugli, T. Elsaesser, and J. Shah, *Phys. Rev. B* **47**, 4226 (1993).
- [10] U. Hohenester, P. Supancic, P. Kocevar, X. Q. Zhou, W. Kütt, and H. Kurz, *Phys. Rev. B* **47**, 13233 (1993).
- [11] C. J. Stanton, D. W. Bailey, and K. Hess, *Phys. Rev. Lett.* **65**, 231 (1990).
- [12] J. Sjakste, K. Tanimura, G. Barbarino, L. Perfetti, and N. Vast, *J. Phys.: Condens. Matter* **30**, 353001 (2018).
- [13] J. Kanasaki, H. Tanimura, and K. Tanimura, *Phys. Rev. Lett.* **113**, 237401 (2014).
- [14] It is true that the temporal evolutions of $f_e(k, E, t)$ are certainly affected by the dynamics of holes generated in the valence band because of the important effects of e-h interactions. However, the holes do not play any role in the photoemission process of excited electrons in the CB in the frame of the quasiparticle picture. When the e-h correlation is strong, as in the case of excitons, the photoemission process is governed by the qualitatively different roles as described in Ref. [15]. We neglect the excitonic effects on photoemission in this paper, as the electrons detected here can be identified clearly to be the quasiparticles in the CB.
- [15] H. Tanimura, K. Tanimura, and P. H. M. van Loosdrecht, *Phys. Rev. B* **100**, 115204 (2019).
- [16] A. Damascelli, Z. Hussain, and Z.-X. Shen, *Rev. Mod. Phys.* **75**, 473 (2003).
- [17] J. A. Sobota, Y. He, and Z.-X. Shen, *Rev. Mod. Phys.* **93**, 025006 (2021).
- [18] H. Tanimura, K. Tanimura, and J. Kanasaki, *Phys. Rev. B* **104**, 245201 (2021).
- [19] H. Tanimura, J. Kanasaki, K. Tanimura, J. Sjakste, N. Vast, M. Calandra, and F. Mauri, *Phys. Rev. B* **93**, 161203(R) (2016).
- [20] M. V. Fischetti and S. E. Laux, *Phys. Rev. B* **38**, 9721 (1988).
- [21] M. Bernardi, D. Vigil-Fowler, J. Lischner, J. B. Neaton, and S. G. Louie, *Phys. Rev. Lett.* **112**, 257402 (2014).
- [22] M. Bernardi, D. Vigil-Fowler, C. S. Ong, J. B. Neaton, and S. G. Louie, *Proc. Natl. Acad. Sci. USA* **112**, 5291 (2015).
- [23] T.-H. Liu, J. Zhou, B. Liao, D. J. Singh, and G. Chen, *Phys. Rev. B* **95**, 075206 (2017).
- [24] H. Tanimura, J. Kanasaki, and K. Tanimura, *Phys. Rev. B* **91**, 045201 (2015).
- [25] B. K. Ridley, *Quantum Processes in Semiconductors* (Oxford University Press, Oxford, 1999).
- [26] I. Vurgaftman, J. R. Meyer, and L. R. Ram-Mohan, *J. Appl. Phys.* **89**, 5815 (2001).
- [27] W. Mönch, *Semiconductor Surfaces and Interfaces* (Springer, Berlin, 1995).
- [28] E. W. Plummer and W. Eberhardt, *Advances in Chemical Physics* (Wiley, New York, 1982).
- [29] K. Oura, V. G. Lifshits, A. A. Saranin, A. V. Zotov, and M. Katayama, *Surface Science: An Introduction* (Springer, Berlin, 2003).
- [30] Ph. Ebert, K. Urban, L. Aballe, C. H. Chen, K. Horn, G. Schwarz, J. Neugebauer, and M. Scheffler, *Phys. Rev. Lett.* **84**, 5816 (2000).
- [31] M. Weinelt, M. Kutschera, R. Schmidt, C. Orth, T. Fauster, and M. Röhlfing, *Appl. Phys. A* **80**, 995 (2005).
- [32] Y.-S. Kim, M. Marsman, G. Kresse, F. Tran, and P. Blaha, *Phys. Rev. B* **82**, 205212 (2010).
- [33] D. W. Niles, D. Rioux, and H. Höchst, *Phys. Rev. B* **46**, 12547 (1992).
- [34] M. T. Portella, J.-Y. Bigot, R. W. Schoenlein, J. E. Cunningham, and C. V. Shank, *Appl. Phys. Lett.* **60**, 2123 (1992).
- [35] To judge whether an electron distribution is quasithermalized or not, we applied a systematic analysis of $f_e(\vec{\Gamma}, E_{ex}, \Delta t)$, paying attention to the two parameters which characterize the spectral shape of the distribution. The first is the peak energy E_{\max} of the distribution, and the other is the asymmetry α_h of the distribution at half the value of the peak amplitude of the distribution. For the spectrum of the Maxwell distribution function convolved with respect to the finite energy resolution ΔE (55 meV in this paper), the mean energy \bar{E}_m is given by $(\frac{3}{2})k_B T_e$ like the case of the original distribution function, but E_{\max} is no longer equal to $k_B T_e/2$; it is a given nonlinear function of \bar{E}_m . Also, the α_h of the convolved Maxwell distribution function is determined theoretically as a function of \bar{E}_m . For the experimental $f_e(\vec{\Gamma}, \bar{E}_{ex}, \Delta t)$, we can evaluate \bar{E}_m using Eq. (1), and E_{\max} and α_h are determined by the shape analysis. Therefore, by comparing the experimental values of E_{\max} and α_h at a given \bar{E}_m with those of the convolved Maxwell distribution functions, we can judge whether the distribution is quasithermalized or nonthermal. The details of the method were described in appendix C of Ref. [18].
- [36] E. M. Conwell and M. O. Vassell, *Phys. Rev.* **166**, 797 (1968).
- [37] A. Mooradian and G. B. Wright, *Solid State Commun.* **4**, 431 (1966).
- [38] G. Fasol, W. Hackenberg, H. P. Hughes, K. Ploog, E. Bauser, and H. Kano, *Phys. Rev. B* **41**, 1461 (1990).
- [39] J. Collet and T. Amand, *J. Phys. Chem. Solids* **47**, 153 (1986).
- [40] P. Lugli, P. Bordone, L. Reggiani, M. Rieger, P. Kocevar, and S. M. Goodnick, *Phys. Rev. B* **39**, 7852 (1989).
- [41] M. A. Osman and D. K. Ferry, *Phys. Rev. B* **36**, 6018 (1987).
- [42] H. Tanimura, J. Kanasaki, K. Tanimura, J. Sjakste, and N. Vast, *Phys. Rev. B* **100**, 035201 (2019).
- [43] H. Tanimura and K. Tanimura, unpublished.
- [44] J. Henk, W. Schattke, H.-P. Barnscheidt, C. Janowitz, R. Manzke, and M. Skibowski, *Phys. Rev. B* **39**, 13286 (1989).
- [45] W. Schattke, *Prog. Surf. Sci.* **64**, 89 (2000).
- [46] M. Lindroos, S. Sahrakorpi, and A. Bansil, *Phys. Rev. B* **65**, 054514 (2002).
- [47] S. Ramakrishna, F. Willing, and K. Knorr, *Appl. Phys. A* **78**, 247 (2004).
- [48] As a cautious note, we comment on some discrepancies between the experimental results and simulated ones. At the low-energy side of the CBM, the intensities of experimental spectra are higher than the simulated spectral intensities, although the differences are small. The difference could be due to donor-induced additional density of states near the CBM characteristic of highly donor-doped samples studied previously in Ref. [37].
- [49] H. C. Casey, Jr. and F. Stern, *J. Appl. Phys.* **47**, 631 (1976).
- [50] C. H. Henry and D. V. Lang, *Phys. Rev. B* **15**, 989 (1977).
- [51] A. M. Stoneham, *Rep. Prog. Phys.* **44**, 1251 (1981).
- [52] H. Sumi, *Phys. Rev. Lett.* **47**, 1333 (1981).
- [53] H. Sumi, *Phys. Rev. B* **27**, 2374 (1983).
- [54] T. N. Theis, B. D. Parker, P. M. Solomon, and S. L. Wright, *Appl. Phys. Lett.* **49**, 1542 (1986).
- [55] M. Isler and D. Liebig, *Phys. Rev. B* **61**, 7483 (2000).
- [56] As the initial states of photoemission must have positive wave vectors along the surface-normal direction, the electrons included in the upper half of detection volume can contribute the photoemission.